Results in Engineering 30 (2026) 109979

Contents lists available at ScienceDirect

Results in Engineering

journal homepage: www.sciencedirect.com/journal/results-in-engineering

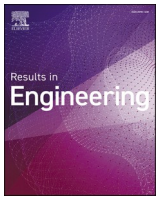

Casson hybrid nanofluid flow between two rotating disks under magnetic field and convective boundary conditions

Sartaj Aziz [a], Hakeem Ullah [a,*], Mehreen Fiza [a], Ilyas Khan [b,c,d], Abdoalrahman S.A. Omer [e,*], Najla A. Mohammed [f], Ibrahim Mahariq [g,h,i,j,*], Ali Akgül [k,l], Farkhod Rakhmonov [m]

[a] Department of Mathematics, Abdul Wali Khan University Mardan, 23200, Khyber Pakhtunkhwa, Pakistan
[b] Department of Mathematical Sciences, Saveetha School of Engineering, SIMATS, Chennai, Tamil Nadu, India
[c] Hourani Center for Applied Scientific Research, Al-Ahliyya Amman University, Amman, Jordan
[d] Széchenyi István University, Győr, Hungary
[e] Department of Information System, College of Computer and Information Sciences, Majmaah University, 11952, Al-Majmaah, Saudi Arabia
[f] Mathematics Department, Faculty of Sciences Umm Al-Qura University, Makkah, Saudi Arabia
[g] College of Engineering and Architecture, Gulf University for Science and Technology, Mishref, Kuwait
[h] Department of Electrical and Electronic Engineering, Faculty of Engineering and Architecture, Istanbul Gelisim University, Avcilar-Istanbul, 34310, Istanbul, Türkiye
[i] Najjad Zeenni Faculty of Engineering, Al-Quds University, Jerusalem, Palestine
[j] University College, Korea University, Seoul 02481, South Korea
[k] Department of Electronics and Communication Engineering, Saveetha School of Engineering, SIMATS, Chennai, Tamil Nadu, India
[l] Siirt University, Art and Science Faculty, Department of Mathematics, 56100 Siirt, Turkey
[m] School of Exact Sciences, National Pedagogical University of Uzbekistan, named after Nizami, Uzbekistan

ARTICLE INFO

Keywords:
Hybrid nanofluid
Joule heating
Casson fluid, rotating stretching disks, bvp4c
Industry innovation and infrastructure
Affordable and clean energy

ABSTRACT

Nanotechnology plays a vital role in heat transport due to its wide range of applications, significantly contributing to fields such as bioengineering, space exploration, biosensor research, semiconductor technology, and advanced electronics. The primary objective of this analysis is to examine the Casson fluid model for heat and mass transport between stretchy rotating disks, incorporating copper and titanium oxide nanoparticles into a sodium alginate base fluid. This analysis encompasses the effects of mixed convection, chemical reactions, convective conditions, activation energy, and thermal radiation. The bvp4c method is utilized to solve the resultant equations. Tables and Figures offer a clear depiction of the results. Understanding the thermal characteristics of hybrid fluids is crucial to energy systems, biological fluid dynamics, and engineering applications, where fluid flow and heat transfer are critical to system performance. At lower disk, the skin friction improved by 10.24% and 12.36% relative to the higher values of the magnetic and Cason parameters. The Schmidt number reduces mass-transfer gradients by 18.1%, whereas the activation energy decreases by 13.7%. The volume fractions of the selected nanoparticles vary from 0.02 to 0.04, and the heat transfer rates for the hybrid nanofluid increases 12% for the hybrid nanofluid as compared to the nanofluid. The hybrid nanofluid significantly affects flow distributions.

1. Introduction

Hybrid nanofluids are typically formed by dispersing nanoparticles in base fluids such as water, oil, or ethylene glycol. Classically, individual nanoparticles may consist of graphene, carbon nanotubes, or other materials known for their exceptionally high thermal conductivity. The presence of two or more nanoparticle types significantly alters the thermal and rheological properties of hybrid nanofluids. Interactions among these nanoparticles change thermophysical properties, thereby enhancing the fluid' s overall thermal performance. Abderahmane et al. [1] explored the three- dimensional dynamics of HNF inside a cubic resonator under a magnetic field. In 1995, Choi et al. [2] introduced the concept of nanofluids, revolutionizing heat transfer science by demonstrating their superior thermal transport capabilities. Mord et al. [3] examined the effects of apparent pressure and viscosity on Al_2O_3/H_2O-based nanofluids, focusing on implications for polymer science and

* Corresponding authors.
E-mail addresses: hakeemullah1@gmail.com (H. Ullah), as.abdoalrahman@mu.edu.sa (A.S.A. Omer), ibmahariq@gmail.com (I. Mahariq).

https://doi.org/10.1016/j.rineng.2026.109979
Received 22 January 2026; Received in revised form 2 March 2026; Accepted 8 March 2026
Available online 9 March 2026
2590-1230/© 2026 The Author(s). Published by Elsevier B.V. This is an open access article under the CC BY-NC-ND license (http://creativecommons.org/licenses/by-nc-nd/4.0/).

climate change models. The combination of nanoparticles improves thermophysical properties by reducing gas bubble size, thereby increasing heat transfer efficiency, as noted by Abu-Nab et al. [4]. This improvement is attributed to the nanoparticles' ability to modify the fluid' s thermal conductivity and other properties, leading to more effective heat transfer in systems such as cooling mechanisms and heat exchangers. The reduced gas bubble radius lowers thermal resistance, thereby optimizing heat transfer performance. Abu-Nab et al. [5] applied the Plesset- Zwick technique to analyze the PRT nanofluid model around an N- dimensional spherical bubble. Research has shown that in nonlinear multi bubble systems, Al_2O_3- water- based nanofluids exhibit increased multi bubble dynamic growth. Furthermore, numerical studies [6,7]have investigated heat and mass transfer in nanofluid flow between two parallel plates, and the results demonstrate strong agreement with existing literature, thereby validating the consistency and accuracy of the findings. Ramesh et al. [8] examined the two- dimensional flow of a Maxwell magneto- nanofluid moving on a stretching surface to investigate the combined action of thermal and concentration boundary layer behavior, convective boundary conditions, and passive nanoparticle volume fraction control. Sheikholeslami et al. [9] investigated magneto- hydrodynamic (MHD) nanofluid flow containing dust particles, incorporating copper nanoparticles in H_2O and kerosene oil as base fluids. Ramesh et al. [10] examined how activation energy and chemical reactions affect the flow of a viscoelastic fluid across a stretching surface. Rashidi et al. [11] investigated the flow of a water-based copper nanofluid.

Rotating magnetohydrodynamic (MHD) flows are based on the principle that magnetic fields can induce electric currents in a moving electrically conductive fluid. Typical examples of such fluids include electrolytes, plasmas, and liquid metals. Magnetohydrodynamic flow can influence different flow systems by exerting a Lorentz force on the fluid. Investigation of magnetohydrodynamic flow has attracted considerable attention in recent years due to its relevance across various fields of science and engineering [12–14]. Ramesh et al. [15] investigated the flow behavior of hybrid carbon nanotubes on a slip surface with an applied magnetic field. The impact of slip on entropy structure in magnetohydrodynamic (MHD) flow over a rotating disk was investigated by Arikoglu et al. [16]. Madhukesh et al. [17] analyzed the dynamics of a steady, incompressible, and magnetized Casson Maxwell non-Newtonian nanofluid in the confinement between two porous disks that are in motion or stationary. Mohanty et al. [18] explored the unsteady 2-dimensional boundary sheet flow of a nanofluid above a stretching/shrinking sheet, including the effects of heat radiation, and found that a rise in nanoparticle concentration improves both velocity and temperature. Nonlinear radiative MHD flows of nanoliquids driven by a rotating disk have been studied [19–22], accounting for the interaction between the conductive fluid and the applied heat flux.

According to theoretical concepts, Joule heating is the generation of heat due to resistive losses during the conversion of electrical energy into thermal energy. Electricity and the design and operation of electrical devices make extensive use of this phenomenon. Allowing for investigation by Reddy et al. [23]. The studies [24,25] analyzed the outcome of Joule heating in Cu/water nanofluid sideways, an extending and constricting chamber, individually. Madhu et al. [26] explored the influences of nonlinear and linear as well as quadratic thermal radiations and activation energy on the flow of a hybrid nanofluid over an oblique stagnation point on a cylinder. According to Yan et al. [27] The dimensionless Eckert number, arising from Joule heating, significantly affects the extension of the thermal boundary layer. Ding et al. [28] Studies of materials with high thermal conductivity, e.g., alumina-based composites, suggest that base-fluid-filled interactions play an important role in determining heat-transfer behaviour and should be accounted for in the analysis of thermal transport in hybrid nanofluids. Chamkha, et al. [29] examined the MHD flow of a hybrid nanofluid (HNF) with the effect of Joule heating and thermal radiation between two parallel plates. Li et al. [30] investigated to focus on determining the influence of the induced magnetic field on the flow of hybrid nanofluid on a stretching surface, which takes into account the endothermic/exothermic reactions between chemicals, and the concentration of discharge of the waste. Li et al. [31] observed the influence of Joule heating on nanofluid movement over a porous channel.

Non-Newtonian fluids are commonly developed across various sectors, including cosmetics, food production, biomedical engineering, and industrial manufacturing. The unique properties of non-Newtonian fluids play an important role in progressing renewable energy and sustainable procedures. The Casson model, a specific non-Newtonian fluid model, exhibits shear-thinning behaviour and stress-dependent characteristics. Ullah et al. [32] examined non-Newtonian fluid flow to investigate the influence of chemical reactions and thermal radiation on an extending sheet within a porous medium. Wajihah et al. [33] explored the rheological properties of blood, with its dilatational behaviour and the development of solid-like layers in non-Newtonian fluid flow with confined channels. They also found that the pulsatile nature of blood flow creates a complex, dynamic environment that significantly affects transient, non-uniform fluid-mechanical conditions. Shamshuddin et al. [34] studied the motion of a non-Newtonian Prandtl-HNFs over a stretching surface, considering the effects of multiple slip conditions and varying chemical reactions. Jeelani et al. [35] examined the behaviour of alumina-copper ethylene-based (MHD) hybrid nanofluid (HNF), flowing above a stretching sheet, with focus on the effects of solar energy and plate suction. The outcomes confirmed that increased solar radiation and stronger magnetic parameters significantly increase the temperature of the HNF flow. Hussain et al. [36] investigated the flow of a non-Newtonian hybrid nanofluid (HNF) over a stretching sheet, accounting for slip effects. The results indicate that fluid velocity decreases as the Casson parameter increases. Reddy et al. [37] studied the behaviour of a non-Newtonian fluid under the influence of an inclined magnetic field. Meenakumari et al. [38] examined the flow of a Casson nanofluid to explore the physical characteristics of convective heat and mass transfer over an extending surface. Ilango et al. [39] investigated the effect of Brownian motion and thermophoresis on the flow of a Casson nanofluid over a stretching sheet, including the influence of an induced magnetic field.

The researchers have significantly contributed to the understanding of heat transfer between coaxial disks under various physical and thermal conditions. The theoretical foundation of the current study is based on findings from numerous numerical calculations and analytical research. Ramzan et al. [40] conducted a comparative study of the nanofluid flow and hybrid nanofluid flow between a pair of rotating coaxial disks. They used the bvp4c solver and Response Surface Methodology (RSM) to obtain numerical solutions to the governing equations. Shehzad et al. [41] studied the magnetohydrodynamic (MHD) flow of an incompressible Maxwell nanofluid over a rotating disk, taking into account the effect of thermophoretic viscous flow within the framework of the CattaneoChristov heat flux model. Their findings revealed that, with increases in the Deborah number and the magnetic parameter, the velocity profiles decrease. Noreen et al. [42] analysed the heat transfer properties of two coaxial disks through the Cattaneoheat flux model of ternary hybrid nanofluids. Their quantitative results indicated that the fluid temperature increased with the thermal radiation parameter. Rehman et al. [43] investigated the flow of a hybrid nanofluid between two rotating, stretchable coaxial disks and examined the effects of various nanoparticle shapes. They reported that increasing the rotational parameter increases tangential velocity, whereas increasing the stretching of the lower disk decreases it. Kumar et al. [44] compared dusty-fluid flow of SWCNTs and MWCNTs suspended in water over a rotating elongated disk with non-uniform heat sources and sinks. Their findings indicate that the SWCNT-based fluid exhibits higher tangential and radial shear stresses and higher heat-transfer rates than the MWCNT-based fluid. Zhang et al. [45] examined MHD flow and heat transfer in a fractional Oldroyd-B nanofluid trapped between two coaxial cylinders using the finite difference method. They found that,

compared with copper, copper oxide, and titanium oxide nanoparticles, silver nanoparticles increase the thermal conductivity of diesel oil. Hayat et al. [46] investigated the heat transfer between coaxial stretchable disks, including Joule heating, thermal stratification, and radiative effects. Ullah et al. [47] extended such models by incorporating advanced physical effects, improving the realism of thermal transport analysis. Lone et al. [48] focused on nanofluids and entropy generation, showing enhanced thermal performance compared to conventional fluids. Alghamdi et al. [49] investigated hybrid nanofluids with magnetic and fractional effects, demonstrating significant improvements in heat transfer efficiency. Sharma et al. [50] provided foundational results on convective heat transfer, which serve as a basis for subsequent studies. Abas et al. [51] incorporated radiation and complex thermophysical properties, with an emphasis on applications in energy and radiation systems. Finally, Hosseinzadeh et al. [52] examined nanofluid flow under complex conditions and confirmed the positive effect of nanoparticles on thermal performance. Sudarmozhi et al. [53] integrated AI-based neural networks with Williamson blood flow models, incorporating Soret Dufour effects and tetra hybrid nanoparticles, demonstrating improved predictive capability for biomedical heat transfer applications. Advanced non-Newtonian and higher-order fluid models were further explored by Ahmad et al. [54], who developed numerical algorithms for fourth-grade nanofluid flow over a Riga plate, demonstrating significant improvements in thermal performance with aluminum alloy nanoparticles. Kapustenko et al. [55] investigated heat transfer enhancement in compact heat exchangers with different channel geometries, confirming that geometric optimization plays a critical role in thermal efficiency. Szűcs [56] employed coupled CFD–FEM simulations to analyze the thermal characteristic length, providing deeper insight into multiphysics heat-transfer modeling. Optimization of thermal systems is addressed by Orosz et al. [57–61] who utilized graph-theoretic approaches for heat exchanger network synthesis, achieving minimum energy consumption and enabling efficient industrial implementation. In applied thermal systems, Kovács et al. [58] studied convective and radiative heat transfer in lithium-ion batteries, highlighting safety and performance implications, whereas Morauszki et al. [59] examined combustion and heat-transfer processes in internal-combustion engines, thereby contributing to energy-system optimization. Szűcs [60] investigated compressibility effects in porous materials, showing their impact on fluid flow and thermal transport behavior in complex media.

After reviewing the literature cited above, the authors assert that the following novelty and objectives are addressed in the model.

1.1. Novelty

The following unique contributions that make this research novel are;

1. A non-Newtonian model (Casson model) was utilized for this study.
2. Copper and titanium oxide nanoparticles dissolved in a sodium alginate base fluid.
3. The MHD and mixed convection effects are incorporated into the momentum equation.
4. Convective boundary conditions are introduced for temperature at the rotating disks.
5. Concentration equation for hybrid nanofluid reported with activation energy term.

1.2. Objectives

The following are the primary goals of the current study:

1. To create a thorough mathematical model for the mixed convection MHD flow of a Casson hybrid nanofluid between two infinitely rotating parallel disks with nanoparticles $(TiO_2 - Cu)$suspended in a sodium alginate (SA) based fluid.
2. To include a variety of realistic physical effects, such as thermal radiation, Brownian motion, thermophoresis, Arrhenius activation energy, Joule heating, magnetic field (Lorentz force), and chemical reaction.
3. To use MATLAB's bvp4c solver to find precise numerical solutions of the resulting boundary value problem.
4. To examine how important dimensionless parameters affect axial and tangential velocities, temperature, and concentration profiles.

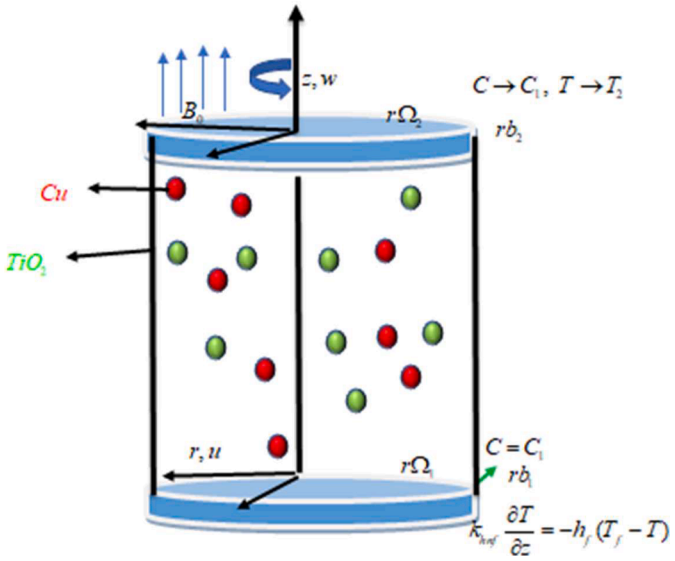

Fig. 1(a). Geometry of the problem.

1.3. Research questions

The following research questions are addressed in this study;

1. How does the mixed convection parameter affect the flow velocity?
2. Which type of nanofluid has a higher heat transfer rate under augmented values of nanoparticles?
3. How do Biot number, Reynold number, and Thermal radiation affect the rate of heat transfer?
4. Which type of nanofluid has superior effects on flow distribution profiles?

2. Statement of problem

Consider the axisymmetric, incompressible, and steady three-dimensional flow of a (HNF) composed of $(TiO_2 - Cu)$ nanoparticles suspended in a base fluid of (SA) between two infinite parallel and rotating disks. The coordinate system (r, θ, and z) has its respective velocities are u, v and w. A consistent magnetic field β_0 is applied in the z-direction, influence the fluid flow. This study integrates Casson hybrid nanofluid, with thermal radiation, and Joule heating in the energy equation while Arrhenius activation function is considered in mass equation to develop the mathematical model. The upper and lower disks stand positioned at $z = h$ *and* $z = 0$ respectively. Furthermore, the angular velocities of the lower and upper disks are represented by $\Omega_1$and $\Omega_2$respectively. It is considered that the fluid is subjected to temperature variations, where the lower disk maintains a surface temperature of T_1while the upper disk at a temperatureT_2. Heat transfer occurs among these surfaces, influencing the thermal performance of the HNF. The

temperature gradient plays an important role in the energy transport mechanism, affecting convection, radiation, and Joule heating effects within the system. The concentration of the lower and upper disks are C_1 and C_2 respectively.the geven coordinate system of cylindricl are use to create the follwing model which show Fig.1(a). Using the above assumptions the governing equation are [42,43,62].

2.1. Continuity equation

$$\frac{1}{r}\frac{\partial}{\partial r}(ru)+\frac{\partial w}{\partial z}=0, \tag{1}$$

Here u, v and w are the velocity components along their respective coordinate's direction in x-axis, y-axis and $z-$ axes.

2.2. Momentum equation

$$u\frac{\partial u}{\partial r}-\frac{v^2}{r}+w\frac{\partial u}{\partial z}=-\frac{1}{\rho_{hnf}}\frac{\partial p}{\partial r}+\frac{\mu_{hnf}}{\rho_{hnf}}\left(1+\frac{1}{\beta}\right)\left(\frac{\partial^2 u}{\partial z^2}+\frac{\partial}{\partial r}\left(\frac{u}{r}\right)+\frac{\partial^2 u}{\partial r^2}\right)$$
$$-\frac{\sigma_{hnf}}{\rho_{hnf}}B_0^2u+\frac{(\rho\beta_T)_{hnf}}{\rho_{hnf}}g(T-T_2), \tag{2}$$

$$u\frac{\partial v}{\partial r}+\frac{vu}{r}+w\frac{\partial v}{\partial z}=\frac{\mu_{hnf}}{\rho_{hnf}}\left(1+\frac{1}{\beta}\right)\left(\frac{\partial^2 v}{\partial z^2}+\frac{\partial}{\partial r}\left(\frac{v}{r}\right)+\frac{\partial^2 v}{\partial r^2}\right)-\frac{\sigma_{hnf}}{\rho_{hnf}}B_0^2v, \tag{3}$$

$$u\frac{\partial w}{\partial r}+w\frac{\partial w}{\partial z}=-\frac{1}{\rho_{hnf}}\frac{\partial p}{\partial z}+\frac{\mu_{hnf}}{\rho_{hnf}}\left(1+\frac{1}{\beta}\right)\left(\frac{\partial^2 w}{\partial z^2}+\frac{1}{r}\frac{\partial w}{\partial r}+\frac{\partial^2 w}{\partial r^2}\right), \tag{4}$$

This equation represents the balance of forces acting on the fluid element. The effect of the magnetic field, the mixed convection term and the Casson model are incorporated. Furthermore, the density of the hybrid nanofluid is denoted by ρ_{hnf}, dynamic viscosity μ_{hnf} and electrical conductivity is σ_{hnf}.

2.3. Temperature equation

$$u\frac{\partial T}{\partial r}+w\frac{\partial T}{\partial z}=\frac{k_{hnf}}{(\rho C_p)_{hnf}}\left(\frac{1}{r}\frac{\partial}{\partial r}\left(r\frac{\partial T}{\partial r}\right)+\frac{\partial^2 T}{\partial z^2}\right)+\frac{1}{(\rho C_p)_{hnf}}\left(\frac{1}{r}\frac{\partial}{\partial r}\left(r\frac{\partial T}{\partial r}\right)+\frac{\partial^2 T}{\partial z^2}\right)\frac{16\sigma^* T_2^3}{3k^*}$$
$$+\frac{(\rho C_p)_{np}}{(\rho C_p)_{hnf}}\left[D_B\left(\frac{\partial T}{\partial z}\frac{\partial C}{\partial z}+\frac{\partial T}{\partial r}\frac{\partial C}{\partial r}\right)+\frac{D_T}{T_2}\left(\left(\frac{\partial T}{\partial z}\right)^2+\frac{1}{r}\frac{\partial T}{\partial r}+\left(\frac{\partial T}{\partial r}\right)^2\right)\right]+\frac{\sigma_{hnf}B_0^2}{(\rho C_p)_{hnf}}(u^2+v^2), \tag{5}$$

This equation represents heat transfer, including Joule heating, thermophoresis, and thermal radiation. Moreover, $D_B$represents the Brownian diffusion coefficient, T is the temperature, and $D_T$means the thermophoretic coefficient. The average absorption coefficient is denoted byk^*, while σ^*represents the Stefan-Boltzmann constant.

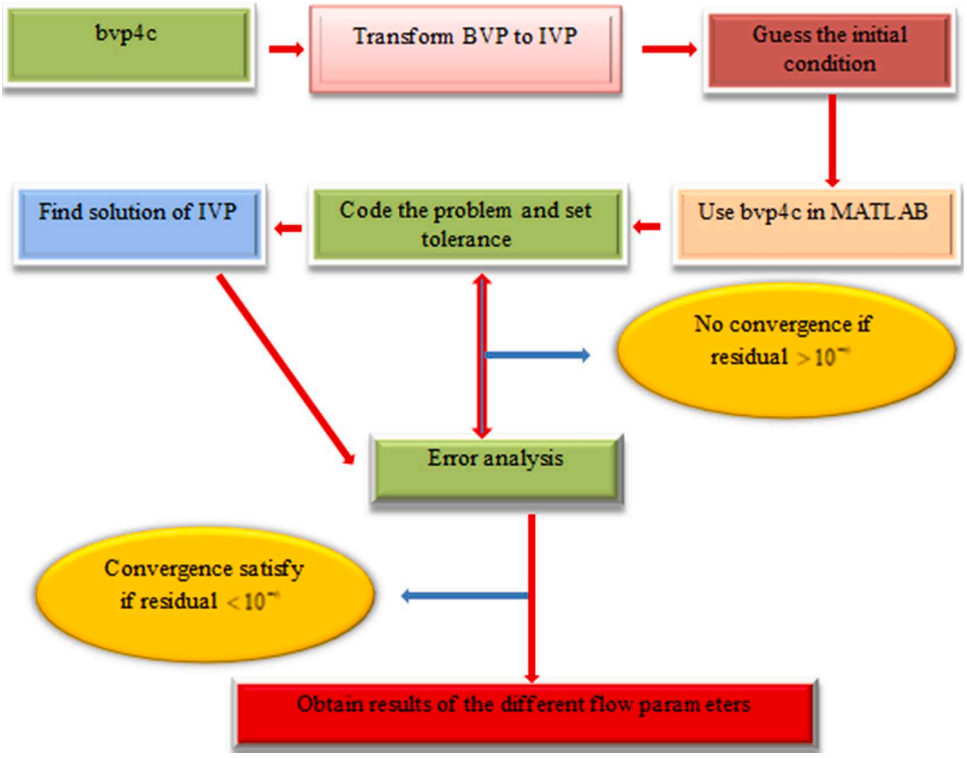

Fig. 1(b). Flow chart of bvp4c.

2.4. Concentration equation

$$u\frac{\partial C}{\partial r}+w\frac{\partial C}{\partial z}=D_B\left(\frac{1}{r}\frac{\partial}{\partial r}\left(r\frac{\partial C}{\partial r}\right)+\frac{\partial^2 C}{\partial z^2}\right)+\frac{D_T}{T_2}\left(\frac{\partial^2 T}{\partial z^2}+\frac{1}{r}\frac{\partial T}{\partial r}+\frac{\partial^2 T}{\partial r^2}\right) -\chi_r\left(\frac{T}{T_2}\right)^n\exp\left(\frac{-E_b}{k_0 T}\right)(C-C_2). \tag{6}$$

It is also known as the mass equation with thermophoretic phenomena and activation energy. Here (C) denotes the concentration of fluid, (χ_r) chemical reaction rate and (C_2) concentration away from the surface.

In Eqs. (1–6) the three velocity components are allied with the cylindrical coordinates (r,θ,z) with$u$, v and w.

2.5. Boundary conditions

The corresponding boundary conditions are defined [47].

$$\left\{\begin{array}{l} u=(b_1 r), v=(\Omega_1 r),\ w=0,\ k_{hnf}\left(\frac{\partial T}{\partial z}\right)=\left(-h_f\left(T_f-T\right)\right),\ C=(C_1),\\ at\ lower\ disk\ z=0,\\ u=(b_2 r),\ v=(r\Omega_2),\ w=0,\ T=T_2,\ C\to C_2\\ at\ upper\ disk\ z=h, \end{array}\right\}. \tag{7}$$

The physical behavior of the boundary conditions of the hybrid nanofluid between two rotating disks is given in Eq. (7). At a lower disk$z$ = 0, the boundary conditions are $u=(b_1 r), v=(\Omega_1 r)$, in which b_1 and $\Omega_1$representing linear stretching and rotation of the lower disk. The boundary condition w = 0shows an impermeable surface with no mass flux. The term $k_{hnf}\left(\frac{\partial T}{\partial z}\right)=\left(-h_f\left(T_f-T\right)\right)$ shows the convective conditions at the surface of the lower disk, which represent the transport of heat from the hot fluid to the disk surface with heat coefficienth_f. Furthermore, at the upper disk $z=h$ the boundary conditions are $u=(b_2 r)$, $v=(r\Omega_2)$ in which b_2 and $\Omega_2$representing linear stretching and rotation of the upper disk. The temperature and concentration of nanoparticles fixed at both disks are $T=T_1$, $C=C_1$ at lower and $T=T_2$, $C=C_2$ at the upper disk, indicating controlled surface temperature and concentration levels.

The thermophysical properties of NFs and HNFs are Lone et al. [48];

$$\left\{\begin{array}{l} \frac{\mu_{hnf}}{\mu_f}=\frac{1}{\left(1-\nabla_{p1}\right)^{5/2}},\\ \frac{\rho_{hnf}}{\rho_f}=\frac{\left[\left(1-\nabla_{p1}\right)\rho_f+\nabla_{p1}\rho_{p1}\right]}{\rho_f},\\ \frac{\sigma_{hnf}}{\sigma_{nf}}=1+\frac{3\left(\frac{\nabla_{p1}\sigma_{p1}}{\sigma_f}-1\right)\nabla_{p1}}{\left(\frac{\nabla_{p1}\sigma_{p1}}{\sigma_f}+2\right)-\left\{\left(\frac{\nabla_{p1}\sigma_{p1}}{\sigma_f}-1\right)\nabla_{p1}\right\}}\\ \frac{k_{hnf}}{k_f}=1+\frac{3\left(\frac{\nabla_{p1}k_{p1}}{k_f}-1\right)\nabla_{p1}}{\left(\frac{\nabla_{p1}k_{p1}}{k_f}+2\right)-\left\{\left(\frac{\nabla_{p1}k_{p1}}{k_f}-1\right)\nabla_{p1}\right\}}\\ \frac{(\rho C_p)_{hnf}}{(\rho C_p)_f}=\frac{\left[\left(1-\nabla_{p1}\right)(\rho C_p)_f+\nabla_{p1}(\rho C_p)_{p1}\right]}{(\rho C_p)_f},\\ \frac{(\rho\beta_T)_{hnf}}{(\rho\beta_T)_f}=\frac{\left[\left(1-\nabla_{p1}\right)(\rho\beta_T)_f+\nabla_{p1}(\rho\beta_T)_{p1}\right]}{(\rho\beta_T)_f} \end{array}\right\}$$

$$\left\{\begin{array}{l} \frac{\mu_{hnf}}{\mu_f}=\frac{1}{\left(1-\nabla_{p1}-\nabla_{p2}\right)^{5/2}},\\ \frac{\rho_{hnf}}{\rho_f}=\frac{\left(1-\nabla_{p2}\right)\left[\left(1-\nabla_{p1}\right)\rho_f+\nabla_{p1}\rho_{p1}\right]+\nabla_{p2}\rho_{p2}}{\rho_f},\\ \frac{\sigma_{hnf}}{\sigma_{nf}}=1+\frac{3\left(\frac{\nabla_{p1}\sigma_{p1}+\nabla_{p2}\sigma_{p2}}{\sigma_f}\right)-3\left(\nabla_{p1}+\nabla_{p2}\right)}{2+\left(\frac{\nabla_{p1}\sigma_{p1}+\nabla_{p2}\sigma_{p2}}{\left(\nabla_{p1}+\nabla_{p2}\right)\sigma_f}\right)-\left\{\left(\frac{\nabla_{p1}\sigma_{p1}+\nabla_{p2}\sigma_{p2}}{\sigma_f}\right)-\left(\nabla_{p1}+\nabla_{p2}\right)\right\}}\\ \frac{k_{hnf}}{k_f}=\frac{\left(\frac{\nabla_{p1}k_{p1}+\nabla_{p2}k_{p2}}{\left(\nabla_{p1}+\nabla_{p2}\right)}\right)+2k_f-2\left(\nabla_{p1}+\nabla_{p2}\right)k_f+2\left(k_{p1}\nabla_{p1}+k_{p2}\nabla_{p2}\right)}{\left(\frac{\nabla_{p1}k_{p1}+\nabla_{p2}k_{p2}}{\left(\nabla_{p1}+\nabla_{p2}\right)}\right)+2k_f+\left(\nabla_{p1}+\nabla_{p2}\right)k_f-2\left(k_{p1}\nabla_{p1}+k_{p2}\nabla_{p2}\right)}\\ \frac{(\rho C_p)_{hnf}}{(\rho C_p)_f}=\frac{\left(1-\nabla_{p2}\right)\left[\left(1-\nabla_{p1}\right)(\rho C_p)_f+\nabla_{p1}(\rho C_p)_{p1}\right]+\nabla_{p2}(\rho C_p)_{p2}}{(\rho C_p)_f},\\ \frac{(\rho\beta_T)_{hnf}}{(\rho\beta_T)_f}=\frac{\left(1-\nabla_{p2}\right)\left[\left(1-\nabla_{p1}\right)(\rho\beta_T)_f+\nabla_{p1}(\rho\beta_T)_{p1}\right]+\nabla_{p2}(\rho\beta_T)_{p2}}{(\rho\beta_T)_f} \end{array}\right\}$$

Here $\nabla$is nanoparticle volume fraction and $p1$, *and* $p2$ stands for first and second nanoparticle.

The similarity variables are defined as [51]:

$$\left.\begin{array}{l} u=(\Omega_1 r f'(\eta)),\quad v=(\Omega_1 r H(\eta)),\quad w=(-2\Omega_1 h f(\eta)),\quad \eta=\left(\frac{z}{h}\right),\\ p=-\rho_f\Omega_1\nu_f\left(P(\eta)+\frac{r^2\in}{2h^2}\right)\left(\theta(\eta)(T_f-T_2)+T_2\right)=T,\quad (\phi(\eta)(C_1-C_2)+C_2)=C. \end{array}\right\} \tag{8}$$

Using the similarity transformation to obtain the flowing odes;

$$\left(1+\frac{1}{\beta}\right)f^{iv}(\eta)+\frac{A_2}{A_1}\mathrm{Re}\left(2f(\eta)f'''(\eta)+2H(\eta)H'(\eta)-\frac{A_3}{A_2}Mf''(\eta)\right)+\frac{A_4}{A_2}Ri\theta'(\eta)=0, \tag{9}$$

$$\left(1+\frac{1}{\beta}\right)H''(\eta)+\frac{A_2}{A_1}\mathrm{Re}\left(2f(\eta)H'(\eta)-2H(\eta)f'(\eta)-\frac{A_3}{A_2}MH(\eta)\right)=0, \tag{10}$$

$$\frac{1}{A_2}P'(\eta)+4\mathrm{Re}f(\eta)f'(\eta)+\frac{2A_1}{A_2}\left(1+\frac{1}{\beta}\right)f''=0, \tag{11}$$

$$\frac{1}{\mathrm{Pr}}\frac{1}{A_6}(A_5+Rd)\theta''(\eta)+\frac{1}{A_6}\left(Nb\theta'(\eta)\phi'(\eta)+Nt(\theta'(\eta))^2\right)+\mathrm{Re}\left(2f(\eta)\theta'(\eta)+EcM\frac{A_3}{A_6}\left((f'(\eta))^2+(H(\eta))^2\right)\right)=0, \tag{12}$$

$$\phi''(\eta)+\mathrm{Re}\left(\begin{array}{c} 2Scf(\eta)\phi'(\eta)+\frac{1}{\mathrm{Re}}\frac{Nt}{Nb}\theta''(\eta)-\\ Sck_r\left((1+\alpha\theta(\eta))^n exp\left(-\frac{E}{1+\alpha\theta(\eta)}\right)\right)\phi(\eta)\end{array}\right)=0, \tag{13}$$

The boundary conditions are:

$$BCs_{(f,H,P,\theta,\phi)}\left\{\begin{array}{l} f(0)=0,\quad f'(0)=\gamma_1,\quad f(1)=0,\quad f'(1)=\gamma_2,\\ H(0)=1,\quad H(1)=\Omega, P(0)=0,\ \phi(0)=1,\\ A_5\theta'(0)=-B_1(1-\theta(0)),\quad \theta(1)=0,\phi(1)=0,\end{array}\right\} \tag{14}$$

In the above equations the dimensionless parameters are, $M=\frac{\sigma_f\beta_0^2}{\rho_f\Omega_1}$is magnetic parameter $\mathrm{Pr}=\frac{(\rho C_p)_f\nu_f}{k_f}$is Prandtl number, $\alpha=\frac{T_f-T_2}{T_2}$ is temperature difference, $Nb=\left(\frac{(\rho C_f)_{np}D_B(C_1-C_2)}{(\rho C_f)_f\nu_f}\right)$is Brownian motion factor, $Sc=\frac{\nu_f}{D_B}$ is Schmidt number, $Nt=\left(\frac{(\rho C_f)_{np}D_T(T_f-T_2)}{(\rho C_f)_f T_2\nu_f}\right)$ is thermophoresis factor, $k_r=\frac{\chi_r h^2}{\nu_f}$ is chemical reaction rate, $Rd=\frac{16\sigma^* T_2^3}{3k^* k_f}$is thermal radiation $E=\frac{E_b}{k_0 T_2}$ is activation energy. $Ec=\frac{h^2{\Omega_1}^2}{(C_p)_f(T_f-T_2)}$ is Eckert number, $\mathrm{Ri}=\frac{Gr}{\mathrm{Re}^2}$ is Richardson number, $Gr=\frac{g\beta_T(T_1-T_2)h^3}{\nu_f^2}$is Grashof number, $B_1=\frac{h_f}{k_f}\sqrt{\frac{\nu_f}{\Omega_1}}$ is Biot number $\mathrm{Re}=\frac{\Omega_1 h^2}{\nu_f}$ is Reynolds number, $\Omega=\frac{\Omega_2}{\Omega_1}$ is a rotation perimeter, $\gamma_2=\frac{b_2}{\Omega_1}$, $\gamma_1=\frac{b_1}{\Omega_1}$ are starching parameters, respectively. Moreover,$A_1=\frac{\mu_{hnf}}{\mu_f}$,$A_2=\frac{\rho_{hnf}}{\rho_f}$,$A_3=\frac{\sigma_{hnf}}{\sigma_f}$, $A_4=\frac{(\rho\beta_T)_{hnf}}{(\rho\beta_T)_f}A_5=\frac{k_{hnf}}{k_f}$, and$A_6=\frac{(\rho C_p)_{hnf}}{(\rho C_p)_f}$are thermophysical constants.

3. Physical quantity

The surface drag forces for both disks are described mathematically as;

$$\begin{array}{l} C_{fx}=\dfrac{\tau_w|_z=0}{\rho_{hnf}(r)^2}, Lower\ disk\\ C_{fx}=\dfrac{\tau_w|_z=h}{\rho_{hnf}(r)^2}, Lower\ disk\end{array} \tag{15}$$

In equation number (18) $\tau_w=\sqrt{\tau_\theta^2 z+\tau_r^2 z}$, with $\tau_{\theta z},\tau_{rz}$are the shear stress respectively at lower disks in radial as well as tangential direction using equation number (8) in (15) we have

$$\begin{array}{l} \tau_{rz}=\left(1+\frac{1}{\beta}\right)\frac{\mu_{hnf}\partial u}{\mu_f\partial z}\Big|_{z=0}=\frac{1}{\mathrm{Re}}\left(1+\frac{1}{\beta}\right)\frac{\mu_{hnf}}{\mu_f}f''(0),\\ \tau_{\theta z}=\left(1+\frac{1}{\beta}\right)\frac{\mu_{hnf}\partial v}{\mu_f\partial z}\Big|_{z=0}=\frac{1}{\mathrm{Re}}\left(1+\frac{1}{\beta}\right)\frac{\mu_{hnf}}{\mu_f}H'(0),\\ \tau_{rz}=\left(1+\frac{1}{\beta}\right)\frac{\mu_{hnf}\partial u}{\mu_f\partial z}\Big|_{z=h}=\frac{1}{\mathrm{Re}}\left(1+\frac{1}{\beta}\right)\frac{\mu_{hnf}}{\mu_f}f''(1),\\ \tau_{\theta z}=\left(1+\frac{1}{\beta}\right)\frac{\mu_{hnf}\partial v}{\mu_f\partial z}\Big|_{z=0}=\frac{1}{\mathrm{Re}}\left(1+\frac{1}{\beta}\right)\frac{\mu_{hnf}}{\mu_f}H'(1),\end{array} \tag{16}$$

Making use of Eq. (16) in Eq. (17)

Lower disk

$$C_{fl}=\mathrm{Re}C_{fx}=\left(1+\frac{1}{\beta}\right)\frac{\mu_{hnf}}{\mu_f}\sqrt{(f''(0))^2+(H'(0))^2}, \tag{17}$$

At upper disk

$$C_{fu}=\mathrm{Re}C_{fx}=\frac{1}{\mathrm{Re}}\left(1+\frac{1}{\beta}\right)\frac{\mu_{hnf}}{\mu_f}\sqrt{(f''(1))^2+(H'(1))^2}, \tag{18}$$

Mathematically the Nusselt number at the lower at the lower and higher disks are express as;

$$\begin{array}{l} Nu_l=\dfrac{hq_w}{k_f(T_f-T_2)}\Big|_{z=0}, Lower\ disk\\ Nu_u=\dfrac{hq_w}{(T_1-T_2)}\Big|_{z=h},\ Upper\ disk\end{array} \tag{19}$$

In Eq. (19) we have

$$q_w=-k_{hnf}\frac{\partial T}{\partial z}\Big|_{z=0}+q_r|_z, \tag{20}$$

Using Eq. (8) in (20) we have;

At lower disk

$$Nu_l=-\left(\frac{k_{hnf}}{k_f}+\frac{4}{3}Rd\right)\theta'(0), \tag{21}$$

At upper disk

Table 1
A comparative analysis of the uniqueness of the envisioned model.

Name	Ramzan et al. [40]	Shehzad et al. [41]	Noreen et al. [42]	Rehman et al. [43]	Kumar et al. [44]	Zhang et al. [45]	Hayat et al. [46]	Present work
Casson model	No	No	No	No	No	No	No	Yes
Mixed convection	No	No	No	No	No	No	No	Yes
Sodium alginate base fluid	No	No	No	No	No	No	No	Yes
Activation energy	No	No	No	Yes	No	No	No	Yes
Convective condition	No	No	No	No	No	No	No	Yes
Rotating disks	Yes	Yes	Yes	Yes	Yes	Yes	Yes	Yes
Bvp4c	Yes	No	Yes	Yes	No	No	No	Yes

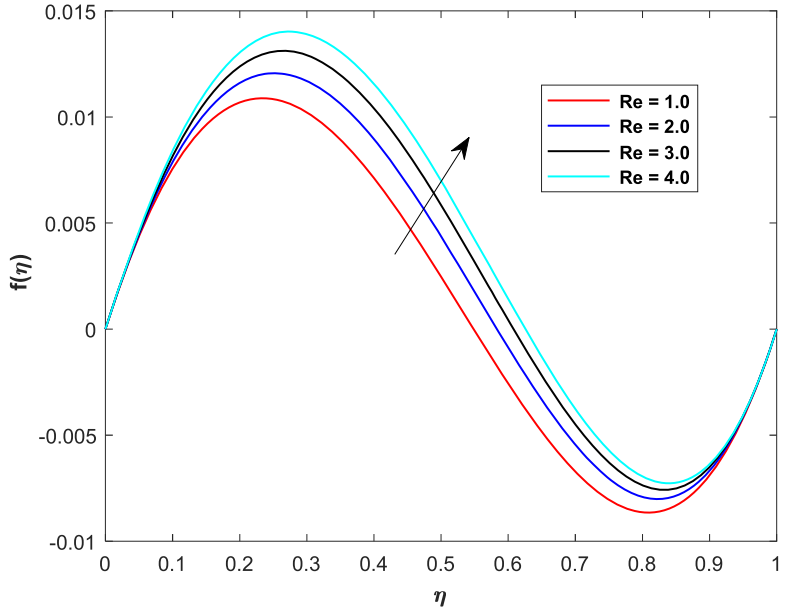

Fig. 2. Influence of Reynold number (Re) on axial velocity ($f(\eta)$), where $\beta = 2.0, M = 0.1, \gamma_1 = 0.4, \gamma_2 = 0.5, Ri = 0.2$.

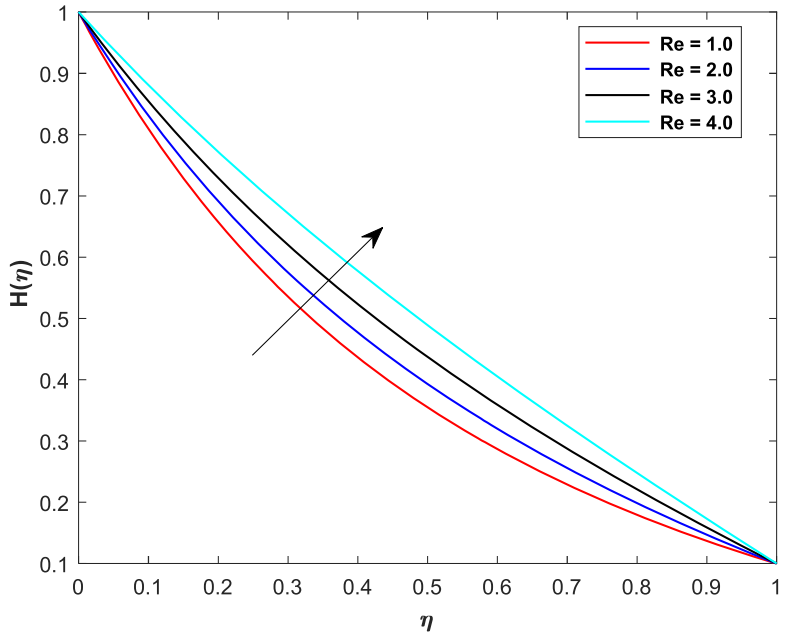

Fig. 3. Influence of Reynolds number (Re) on tangential velocity$H(\eta)$, where $\beta = 2.0, M = 0.1, \gamma_1 = 0.4, \gamma_2 = 0.5, \Omega = 1.0$.

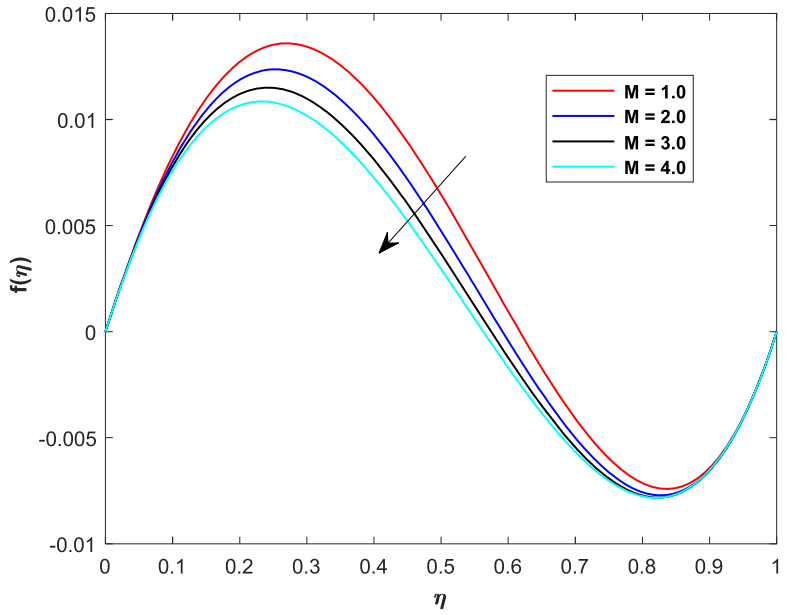

Fig. 4. Influence of magnetic field parameter (M) on velocity profile $f(\eta)$,where $\beta = 2.0, \mathrm{Re} = 2.1, \gamma_1 = 0.4, \gamma_2 = 0.5, Ri = 0.2$.

$$Nu_u = -\left(\frac{k_{hnf}}{k_f} + Rd\right)\theta'(1), \tag{22}$$

For the hybrid nanofluid Sherwood number are define as;

$$\left[Sh_x = -\frac{hq_m}{D_B(C_2 - C_1)}\right], \tag{23}$$

Where q_m is the mass flux which is define as;

$$q_m|_z = -D_B \frac{\partial C}{\partial z}\Big|_{z=0}. \tag{24}$$

Thus the Sherwood number is reduced as;

$$Sh_{xl} = -\phi'(0) \tag{25}$$

At upper disk

$$Sh_{xu} = -\phi'(1) \tag{26}$$

$\mathrm{Re} = \frac{\Omega_1 h^2}{\nu_f}$is local Reynolds number.

4. Numerical procedure

In this study, we utilize MATLAB's bvp4c numerical solver to solve the structure of non-linear ODEs subject to the boundary conditions. The bvp4c method is applied across a range of governing parameter values to comprehensively investigate the problem. Set the absolute and relative tolerance $10^{-6}$for the results below to ensure the accuracy and maintain computational efficiency. The flow chart of bvp4c method is given in Fig. 1(b).

Key Features of bvp4c;

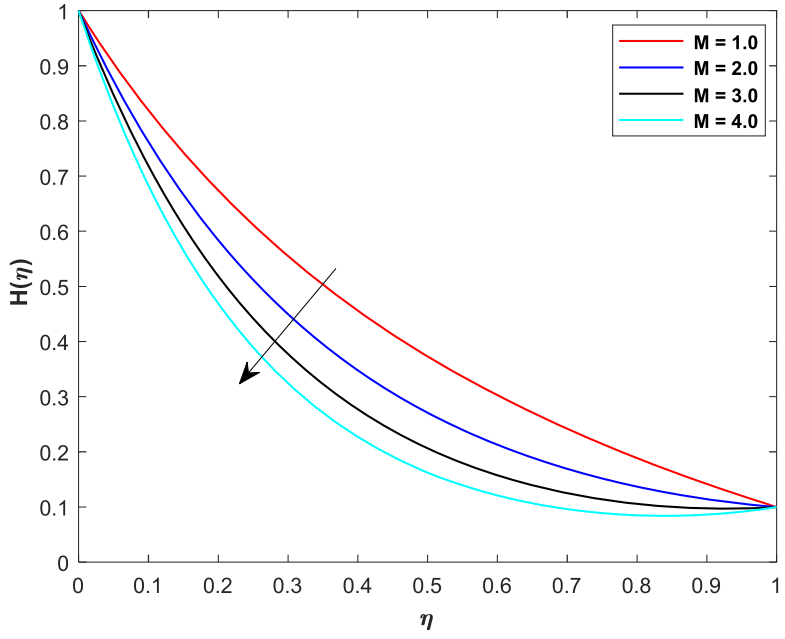

Fig. 5. Influence of magnetic field parameter (M) on tangential velocity $H(\eta)$,where $\beta = 2.0, \mathrm{Re} = 2.1, \gamma_1 = 0.4, \gamma_2 = 0.5, \Omega = 1.0$.

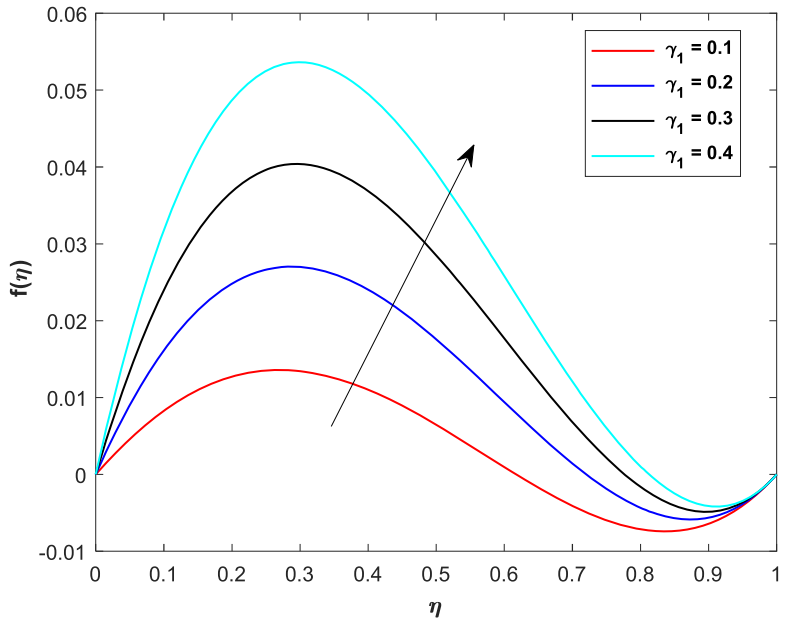

Fig. 6. Influence of stretching ratio parameter (γ_1) on velocity profile$f(\eta)$. Where $\beta = 2.0, M = 0.1, Ri = 0.3, \gamma_2 = 0.5, \mathrm{Re} = 2.1$.

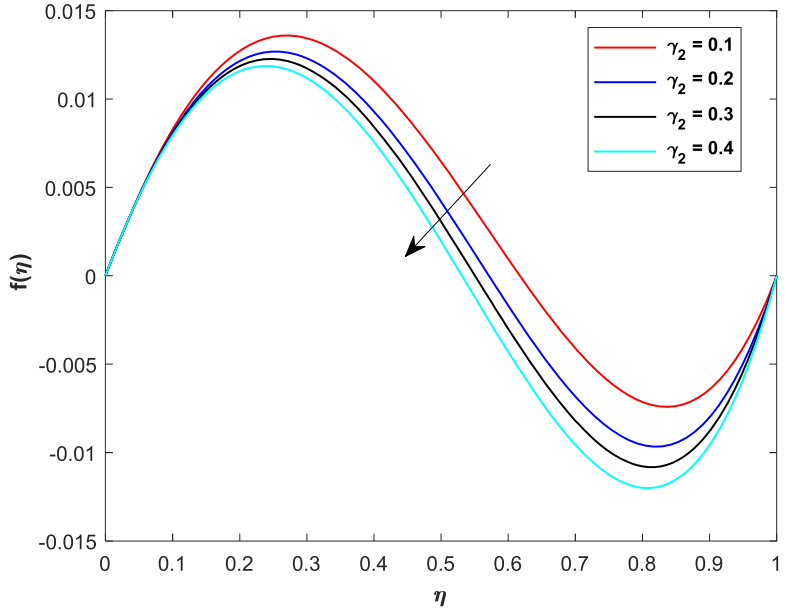

Fig. 7. Influence of stretching ratio parameter (γ_2) on velocity profile$f(\eta)$. Where $\beta = 2.0, M = 0.1, Ri = 0.3, \gamma_1 = 0.5, \mathrm{Re} = 2.1$.

- ➢ Solves both linear and nonlinear boundary value problems.
- ➢ Uses adaptive mesh refinement.
- ➢ Efficient for smooth solutions.

$$\begin{array}{lll} y(1)=f(\eta), & y(5)=H(\eta), & y(9)=\theta'(\eta), \\ y(2)=f'(\eta), & y(6)=H'(\eta), & y'(9)=\theta''(\eta), \\ y(3)=f''(\eta), & y'(6)=H''(\eta), & y(10)=\phi(\eta), \\ y(4)=f'''(\eta), & y(7)=P(\eta), & y(11)=\phi'(\eta), \\ y(4)=f'''(\eta), & y'(7)=P'(\eta), & y'(11)=\phi''(\eta), \\ y'(4)=f''''(\eta), & y(8)=\theta(\eta), & \end{array} \tag{27}$$

$$y'(4) = -\frac{A_2}{A_1}\left(\mathrm{Re}\left(2y(1)y(4)+2y(5)y(6)-\frac{A_3}{A_2}My(3)\right) + \frac{A_4}{A_2}Riy(8)\right) \Big/ \left(1+\frac{1}{\beta}\right), \tag{28}$$

$$y'(6) = -\frac{A_2}{A_1}\mathrm{Re}\left(2y(1)y(6)-2y(5)y(2)-\frac{A_3}{A_2}My(5)\right) \Big/ \left(1+\frac{1}{\beta}\right), \tag{29}$$

$$y'(7) = -4A_2\mathrm{Re}y(1)y(2) - 2A_1\left(1+\frac{1}{\beta}\right)f(3) \tag{30}$$

$$-\frac{1}{A_6}\left(Nby(9)y(11)+Nt(y(9))^2\right)$$

$$y'(9) = \frac{-\mathrm{Re}\left(2y(1)y(9)+EcM\frac{A_3}{A_6}\left((y(2))^2+(y(5))^2\right)\right)=0,}{\frac{1}{\mathrm{Pr}}\frac{1}{A_6}(A_5+Rd)} \tag{31}$$

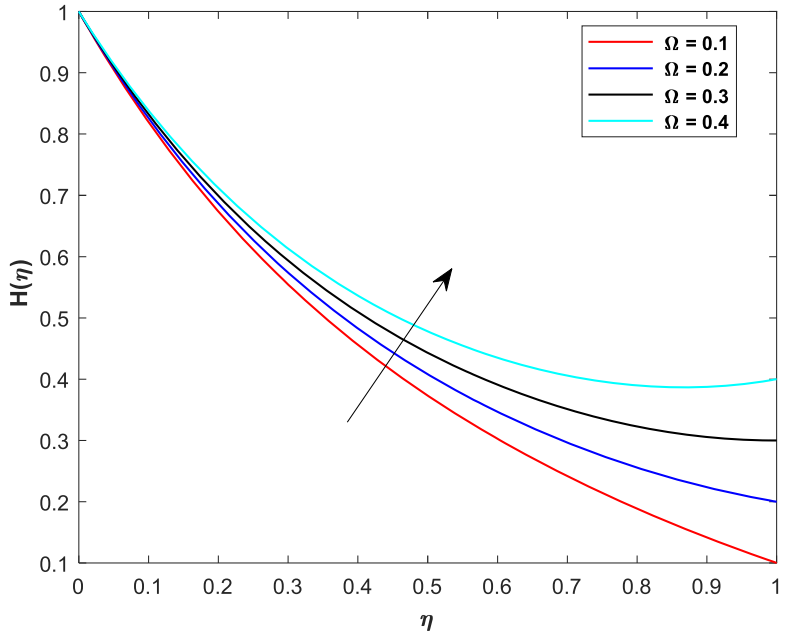

Fig. 8. Influence of rotation parameter Ω on tangential velocity $H(\eta)$,where $\beta = 2.0, \mathrm{Re} = 2.1, M = 0.3, \gamma_1 = 0.4, \gamma_2 = 0.5, \Omega = 1.0$.

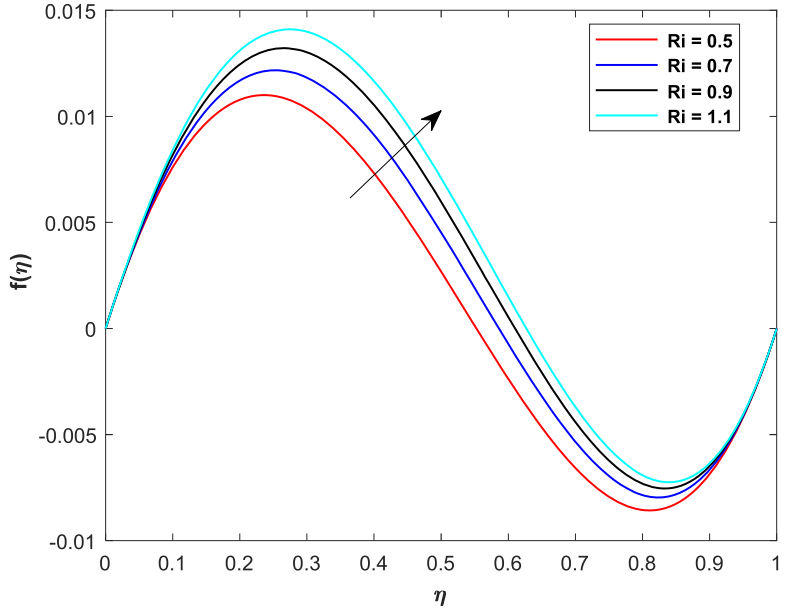

Fig. 9. Influence of convective parameter (Ri) on velocity profile$f(\eta)$,where $\beta = 2.0, M = 0.1, \gamma_1 = 0.4, \gamma_2 = 0.5, Rd = 0.4, \mathrm{Re} = 2.1$.

$$y'(11) = -\mathrm{Re}\left(2Scy(1)y(11) + \frac{1}{\mathrm{Re}}\left(\frac{Nt}{Nb}\right)y'(9) - Sck_r(1+\alpha y(8))^n \exp\left(-\frac{E}{1+\alpha y(8)}\right)y(10)\right) \tag{32}$$

The following are the newly modified boundary conditions:

$$y_a(1) - 0,\ y_a(2) - \gamma_1\ \ y_b(1) - 0,\ y_b(2) - \gamma_2\ \ y_a(5) - 1, y_b(5) - \Omega,\\ y_a(7) - 0,\ A_5 y_a(9) + B_1(1 - y_a(8)), y_b(8) - 0, y_b(10) - 0, y_b(10) - 0. \tag{33}$$

5. Validation

This section includes the validation of the present work with the published work in the literature to show the accuracy of the model. Table 1 Table 3 shows the comparative results of $f''(0)$and $-g'(0)$with the work published by Hosseinzadeh et al. [52]. These results show a close agreement with the published one, which provide evidence for the validation of the present work.

6. Results and discussion

This section presents graphical representations of fluid profiles for numerous key parameters, accompanied by brief details for better clarity. The governing flow equations are transformed into a system of ordinary differential equations (ODEs) using suitable similarity trans-

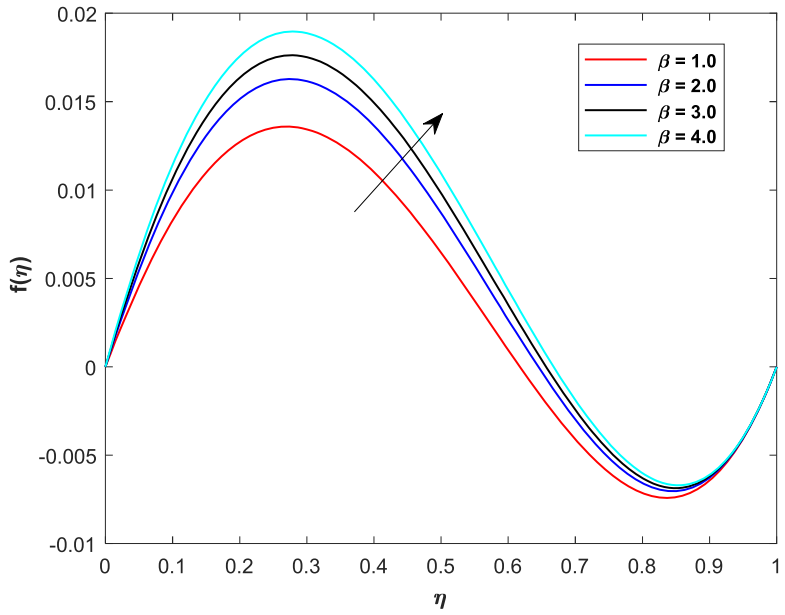

Fig. 10. Influence of Casson parameter (β) on velocity profile$f(\eta)$. Where $M = 0.3, \mathrm{Re} = 2.0, \gamma_1 = 0.4, \gamma_2 = 0.5, Ri = 0.1$.

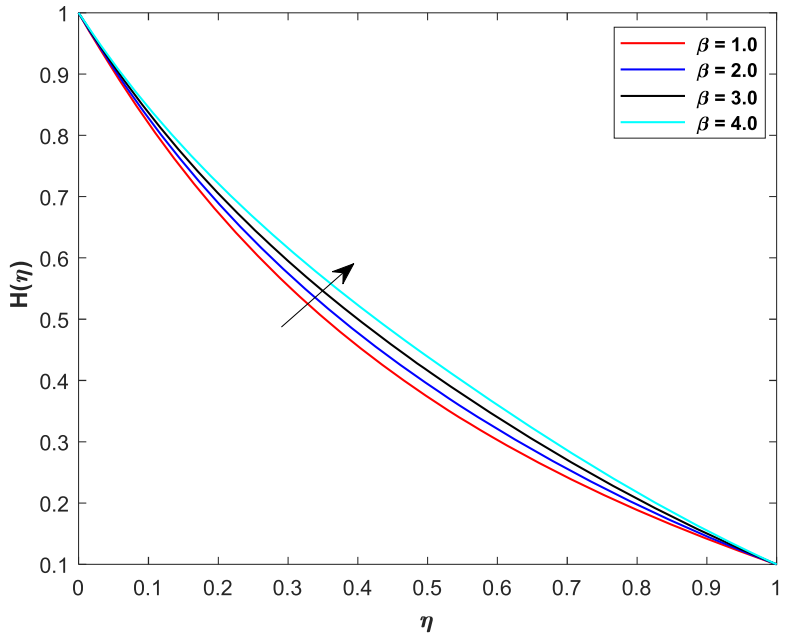

Fig. 11. Influence of Casson parameter (β) on velocity profile$H(\eta)$. Where $M = 0.3, \mathrm{Re} = 2.1, \gamma_1 = 0.4, \gamma_2 = 0.5, Ri = 0.1$.

formations. The resulting ODEs are then solved numerically using the bvp4c method in MATLAB. The investigation achieve for magnetic perimeter (M), Reynolds number (Re), Schmidt number (Sc), Eckert number (Ec), Mixed convective parameter (Ri), chemical reaction (k_r)Brownian motion (Nb), activation energy (E), Biot number (B_1) thermophores factor (Nt), Prandtl number (Pr), rotation parameter (Ω), stretching parameters (γ_1, γ_2), Casson parameter, (β) on axial and tangential velocities, ($f(\eta)$),($H(\eta)$), temperature, ($\theta(\eta)$), and concentration profile ($\phi(\eta)$).

6.1. Velocities distributions

Fig. 2 shows the consequences of Reon$f(\eta)$. This Figure shows a rise in $f(\eta)$ is disclosed with an increase inRe. The augmentation of the Reynolds number is physically linked to the predominance of inertial forces over viscous resistance, facilitating a more unrestricted axial movement of the fluid. At elevatedRe, increased fluid inertia amplifies momentum transfer, resulting in rapid axial flow, as illustrated in Fig. 2. Furthermore, the increase in tangential velocity $H(\eta)$is attributed to less viscous damping at elevatedRe, which allows rotational effects to amplify and augment circumferential fluid motion, as illustrated in Fig. 3. Fig. 4 visualize the impact of Mon$f(\eta)$. The intensification in M declines$f(\eta)$. Physically magnetic field ascribed to the Lorentz force, which counteracts the velocity of the electrically conductive fluid and diminishes axial momentum. The magnetic dampening effect enhances flow resistance, resulting in a decrease in axial flow, as illustrated in Fig. 4. Correspondingly, the tangential velocity $H(\eta)$diminishes as a result of magnetic resistance that opposes rotational motion and dissipates kinetic energy, as elucidated in Fig. 5. Fig. 6 depicts the effect of γ_1 on$f(\eta)$. This Figure demonstrates an increasing trend in $f(\eta)$ with the rise

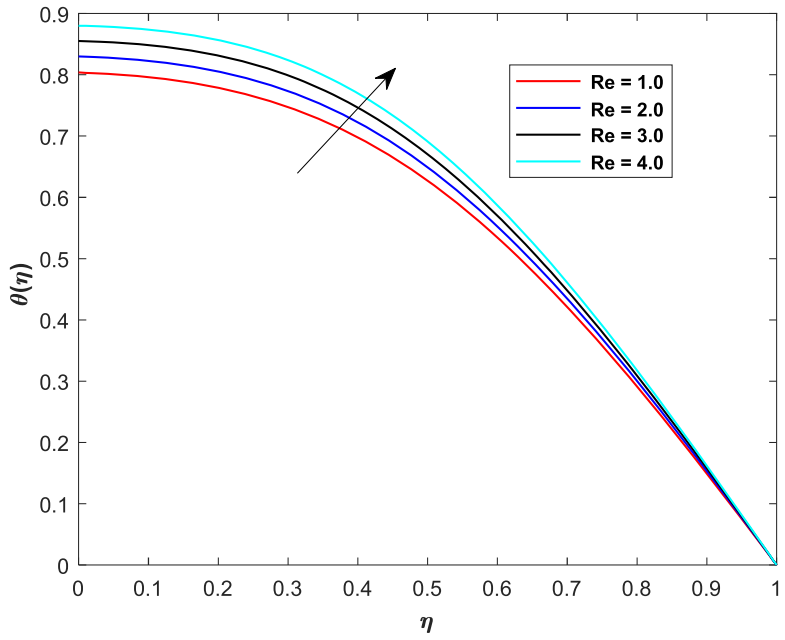

Fig. 12. Influence of Reynolds number (Re) on temperature profile$\theta(\eta)$, where $\beta = 2.0, M = 0.1, Nt = 0.3, Rd = 0.4, B_1 = 0.6, Ec = 0.5, Nb = 0.2$.

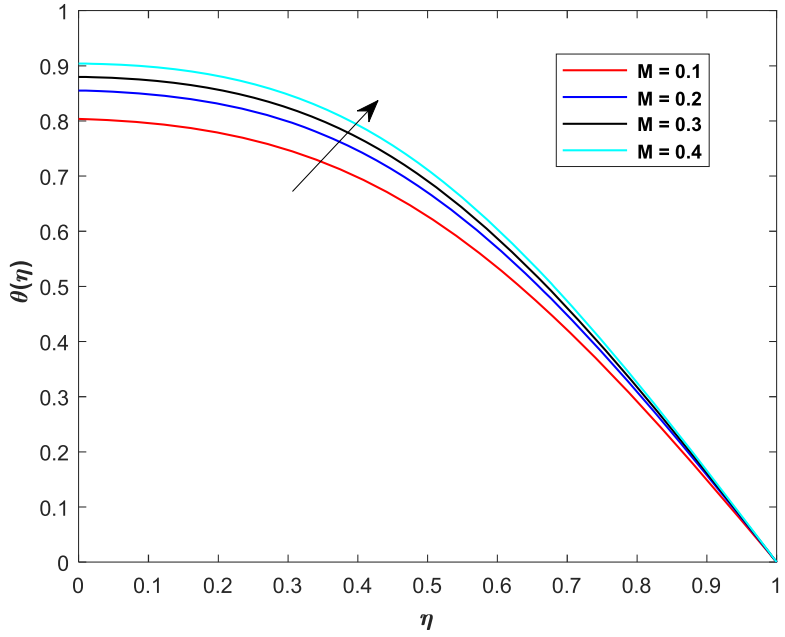

Fig. 13. Influence of magnetic field parameter M on temperature profile $\theta(\eta)$,where $\beta = 2.0, \mathrm{Re} = 0.1, Nt = 0.3, Rd = 0.4, B_1 = 0.4, Ec = 0.5, Nb = 0.2$.

ofγ_1. This increase in $f(\eta)$with growth $\gamma_1$can be physically interpreted as a result of the intensified pulling action exerted by the stretched surface on the fluid. As the stretching factor escalates, the surface of the lower disk expands more swiftly, transferring increased momentum to the neighbouring fluid layers. The augmented momentum transfer enhances the fluid motion in the axial direction, resulting in an elevation off(η). The consequences of $\gamma_2$on $f(\eta)$is dipected in Fig. 7. This decrease in $f(\eta)$with the increase inγ_2, physically ascribed to the redistribution of fluid momentum resulting from enhanced surface stretching. As the upper disk undergoes increased stretching, it facilitates augmented radial fluid motion along the disk surface. The augmented radial transport redirects momentum from the axial direction and modifies the pressure distribution between the disks. As a result, the resistance to axial motion escalates, diminishing the axial flow and causing a significant decrease in $f(\eta)$over the flow region. Fig. 8 is shows the impression of Ω on $H(\eta)$. The increase in $H(\eta)$with the enhancement of Ω is attributable to the intensified rotational motion exerted by the disks on the fluid. As Ω increases, the fluid adjacent to the disk surface undergoes heightened circumferential acceleration, hence augmenting momentum in the tangential direction. The augmented rotational energy is conveyed by viscous forces to neighbouring fluid layers, amplifying the overall tangential motion. Consequently, increased rotation enhances the swirling flow, intensifies centrifugal effects, and elevates the influence of disk rotation on circumferential fluid dynamics. The scattering of the Ri on$f(\eta)$ of HNF is shown in Figs. 9. A higher (Ri) increases the fluid velocity because it increases the buoyancy force ($Ri \propto Gr$), which in turn affects the fluid's speed because of the combined effects of the temperature gradient ratio and inertial forces. Fig. 10

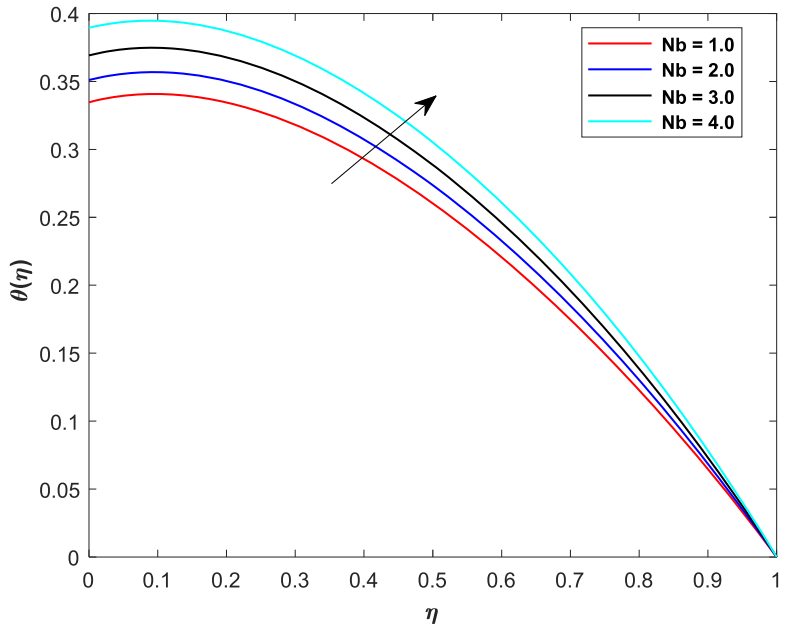

Fig. 14. Influence of Brownian motion (Nb) on temperature profile $\theta(\eta)$,where $\beta = 2.0, M = 0.1, Nt = 0.3, Rd = 0.4, B_1 = 0.6, Ec = 0.5, \mathrm{Re} = 0.2$.

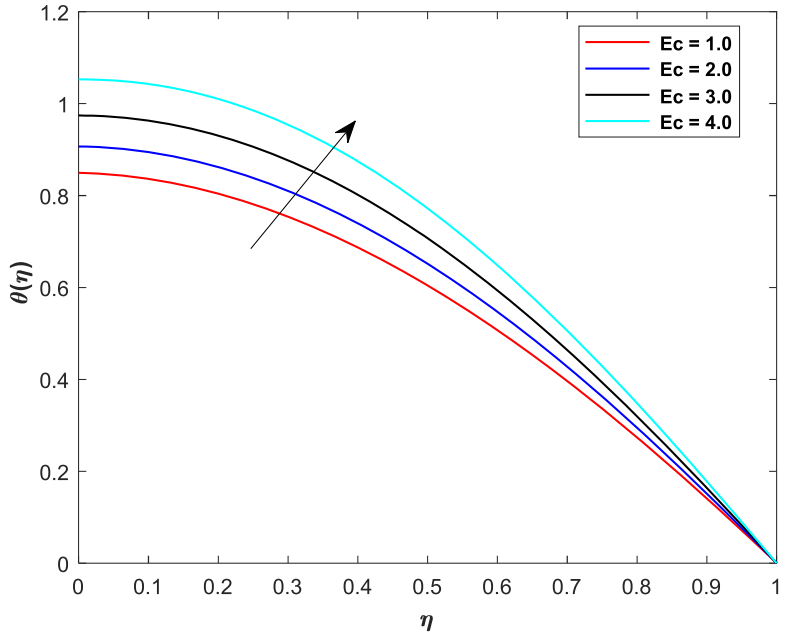

Fig. 15. Influence of Eckert number (Ec) on temperature profile $\theta(\eta)$,where $Nt = 0.3, \beta = 2.0, \mathrm{Re} = 0.4, Rd = 0.6, M = 0.3, B_1 = 0.5, Nb = 0.2$.

illustrate the variance in $f(\eta)$ as a function ofβ . The results indicate that $f(\eta)$ rise with the rising β factor. Due to the introduction of tensile stress, the thickness of the boundary layer diminishes as the Casson factor increases. The increase in yield stress associated with the βsubsequently enhances$f(\eta)$. The same effect is seen in $H(\eta)$against higher values of β in Fig. 11.

6.2. Temperature profiles

The influence of several parameters on thermal profiles $\theta(\eta)$ is seen in Figs. 12–19.

Fig. 12 illustrates the impact of Re on the temperature profile. Higher Reynolds number indicates stronger inertial forces. This leads to a rise in fluid velocity and improved viscous debauchery. Viscous dissipation converts kinetic energy into thermal energy, affecting an increase in temperature within the fluid the thermal $\theta(\eta)$profile boosts. Increased fluid velocity and stronger viscous dissipation are the results of inertial forces predominating over viscous forces, as shown by higherRe. This mechanism raises the fluid's temperature by converting kinetic energy into thermal energy, $\theta(\eta)$increases. This is due to improved viscous dissipation higher velocity gradients change more kinetic energy into thermal energy via internal friction. This self-heating machinery is dangerous in high-speed rotating machinery where cooling efficiency must balance frictional heating. Fig. 13 shows the outcome of M on$\theta(\eta)$of the $TiO_2 - Cu/Ag$ of Hybrid nanofluid. An improvement in the temperature profile is noted with increasing magnetic intensity. Physically, a stronger magnetic field increases the resistance experienced by fluid particles, which leads to greater energy dissipation and

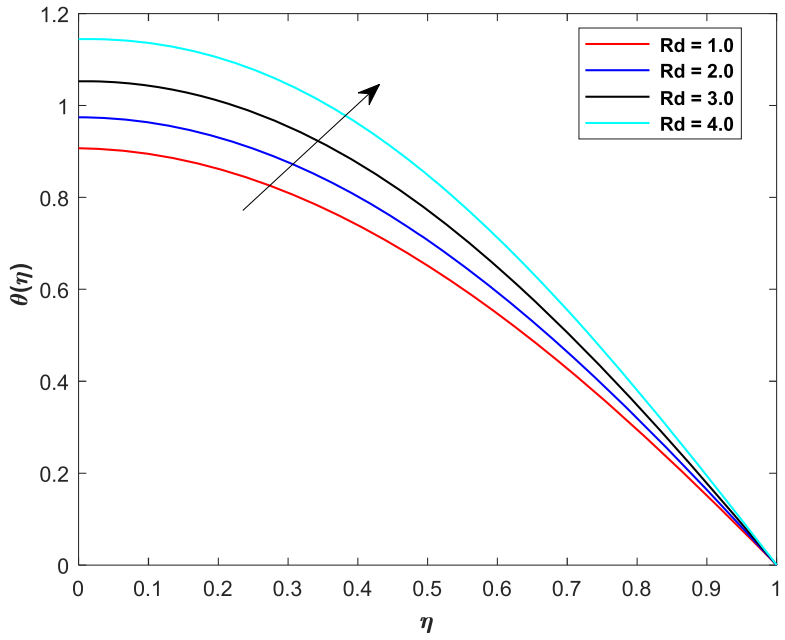

Fig. 16. Influence of thermal radiation Rd on temperature profile $\theta(\eta)$,where $Nt = 0.3, Ec = 0.6, M = 0.3, B_1 = 0.6, \beta = 2.0, Nb = 0.2$.

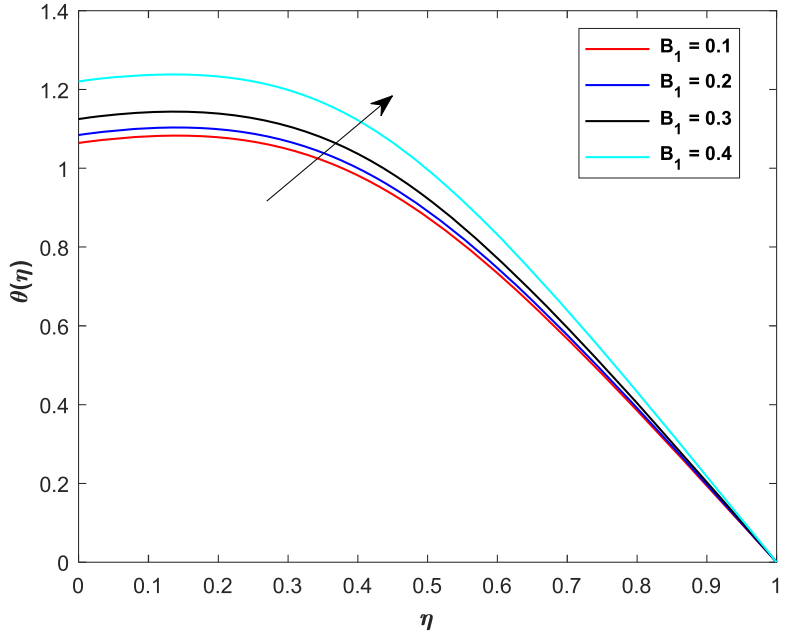

Fig. 17. Influence of thermal radiation B_1 on temperature profile $\theta(\eta)$,where $Nt = 0.3, \mathrm{Re} = 2.1, Ec = 0.6, M = 0.3, Rd = 0.5, Nb = 0.2$.

consequently elevates the temperature distribution. Fig. 14 shows the effects of *Nb* on$\theta(\eta)$. The temperature profile $\theta(\eta)$ is established to improve as *Nb* values rise. The increased random motion of nanoparticles at explains this behavior greater*Nb*, which improves the fluid's tiny energy transmission. The flow's thermal properties are strengthened because of the nanoparticles' internal energy being more successfully transformed into thermal energy. Therefore, as Fig. 14 makes evident, an increase in the Brownian motion parameter directly leads to increased temperature distributions. The influence of *Ec* on $\theta(\eta)$is seen in Fig. 15, demonstrating an increase in $\theta(\eta)$ corresponding to a rise in*Ec*. The increase in $\theta(\eta)$ with the enhancement of*Ec*, physically elucidated as a result of heightened viscous dissipation inside the fluid. An elevated *Ec* signifies that the kinetic energy of the fluid is being transformed more efficiently into internal energy as a result of viscous processes. This process produces more heat, elevating the fluid temperature. As a result, the fluid absorbs additional energy, leading to an increase in temperature distribution. This effect is primarily significant in high-speed or high-viscosity flows, when viscous heating greatly impacts thermal transport and energy properties. The effect of the radiation parameter (Rd)on the temperature profile $\theta(\eta)$ is seen in Fig. 16. Thermal radiation contributes an additional heat flux following the Roseland approximation. The temperature rises when (Rd) increases. Physically, radiative heat transmission becomes more intense as the (Rd) parameter rises, giving the working fluid greater thermal energy. As the coordination engages added heat after radiative bases, the fluid hotness increases owed to this extra energy. The impression of B_1 on $\theta(\eta)$is shown in Fig. 17. Growth in B_1 intensify the $\theta(\eta)$distribution. Mathematically, $B_1 = \frac{h_f}{k_f}\sqrt{\frac{\nu_f}{\Omega_1}}$, which shows that $B_1$is related to heat transfer coefficient h_f

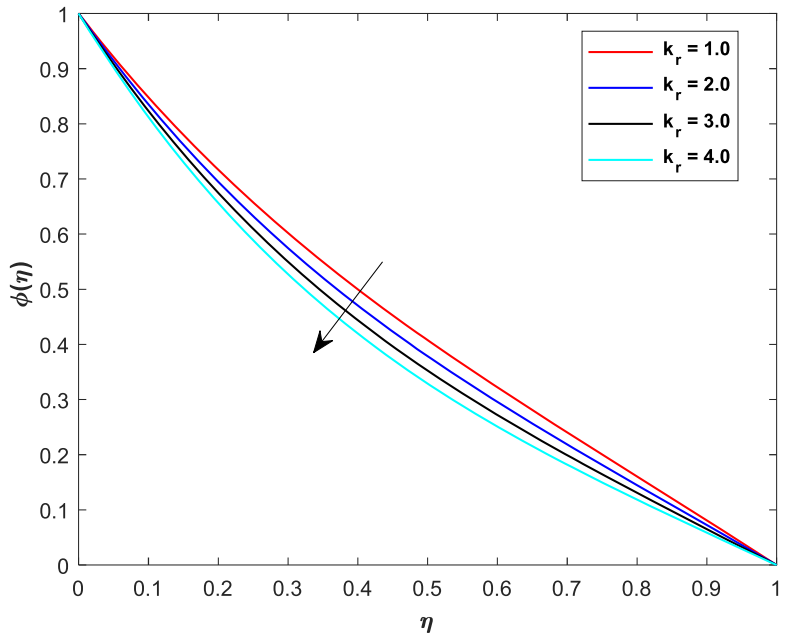

Fig. 18. Influence of chemical reaction rate k_r on concentration profile$\phi(\eta)$. Where $Nt = 0.3, \mathrm{Re} = 2.1, Sc = 0.1, E = 0.6, Nb = 0.2$.

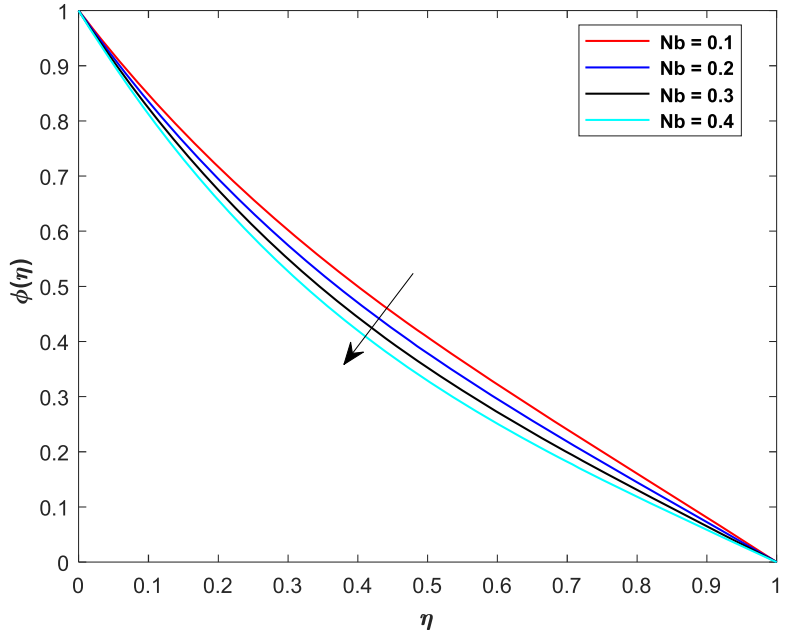

Fig. 19. Influence of Brownian motion Nb on concentration profile $\phi(\eta)$,where $Nt = 0.3, \mathrm{Re} = 2.1, Sc = 0.1, E = 0.6, k_r = 0.2$.

. Higher values of B_1 amplifies the thermal transport which significantly esclates the $\theta(\eta)$.

6.3. Concentration profile

Fig. 18 illustrates the influence of k_r on $\phi(\eta)$. From this here, we deduced that the greater k_r diminishes$\phi(\eta)$. Higher values of k_r diminish the boundary layer thickness of a nanoparticle distribution. The decrease in the boundary layer leads to a diminished distribution of nanoparticle concentration. Fig. 19 illuminates the outcome of the Nb on the$\phi(\eta)$. Brownian motion rises to random nanoparticle movement, while thermophoresis is particle migration due to temperature gradients. As Nb increases, the concentration profile decreases. Higher values of Nb increase the random motion of nanoparticles, which decreases quantity dispersion and weakens the solutal absorption. The impact of the Sc on the concentration field of hybrid nanofluids is seen in Fig. 20. Mass diffusivity decreases with increasingSc, resulting in a drop in $\phi(\eta)$profile. A greater concentration gradient in the fluid results from higher Sc values, which signify lower molecular diffusion rates. Fig. 21 illustrates the effect of E on $\phi(\eta)$. This Figure indicates that a higher Eincreases$\phi(\eta)$. Higher values of E augment the boundary layer thickness of a nanoparticle distribution. This increase in the boundary layer leads in an amplified distribution of nanoparticle concentration. As a result $\phi(\eta)$distribution enhanced with E.

6.4. Comparison graphs

A comparative examination of the nanofluid and hybrid nanofluid on

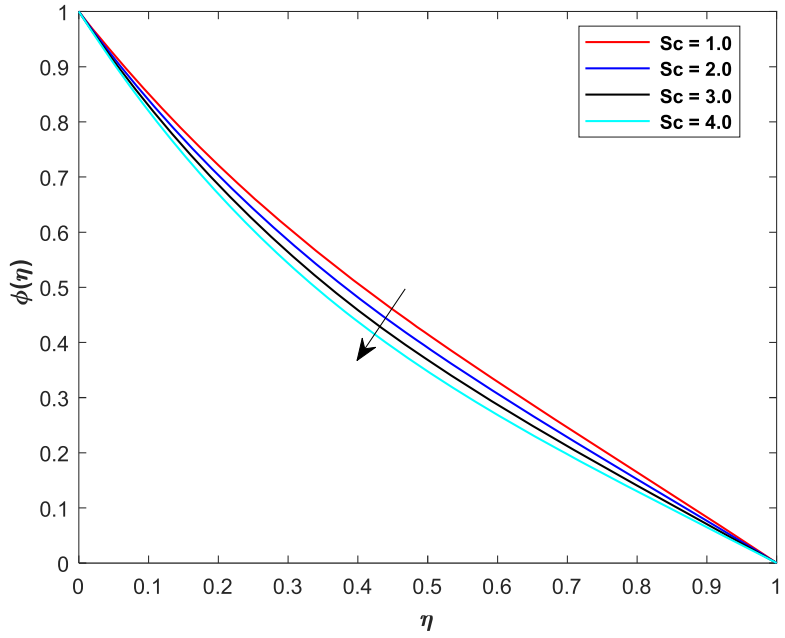

Fig. 20. Influence of Schmidt number (Sc) on concentration profile $\phi(\eta)$,where $Nt = 0.3, \mathrm{Re} = 2.1, k_r = 0.6, Ec = 0.6, E = 0.5, Nb = 0.2$.

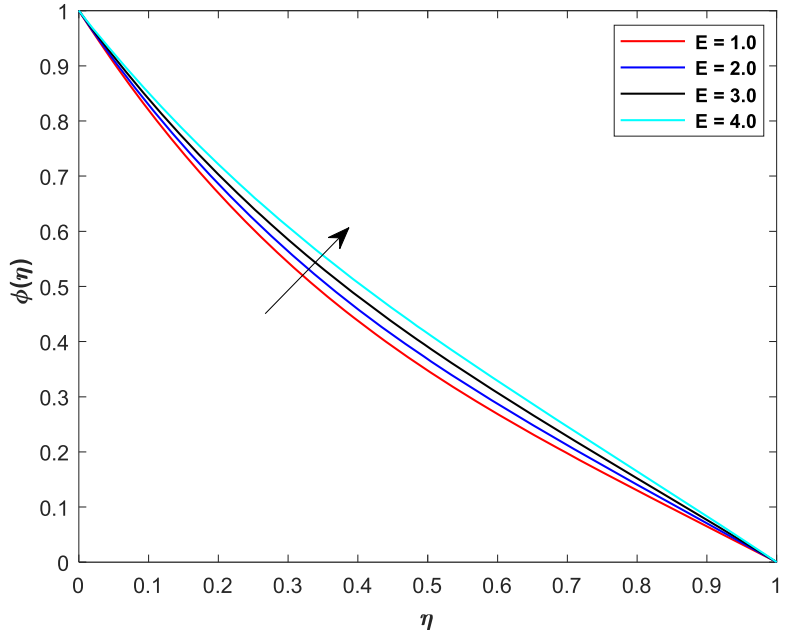

Fig. 21. Influence of activation (E) on concentration profile $\phi(\eta)$,where $Nt = 0.3, \mathrm{Re} = 2.1, k_r = 0.6, Ec = 0.6, Sc = 0.5, Nb = 0.2$.

velocities and temperature concentration profiles is presented in Fig. 22. Hybrid nanofluids exhibit a more pronounced alteration in velocity fields than mono-fluids due to their enhanced effective thermal conductivity and modified rheological properties, indicating superior momentum transport capacity and flow regulation Fig.23. The axial and tangential velocities often increase with nanoparticle complexity Fig.24 due to enhanced energy-exchange mechanisms. The hybrid nanofluids demonstrate significant improvements in thermal characteristicsFig.25, attributable to enhanced heat-transfer efficiency arising from elevated thermal conductivity and improved microscale energy diffusion. Conversely, concentration profiles demonstrate steeper gradients in hybrid nanofluids, attributable to enhanced mass diffusivity and the interaction between particles and fluids. The results demonstrate that hybrid nanofluids outperform than nanofluid.

6.5. Table discussion

Table 2 delineates the numerical values of thermophysical properties. Table 3 presents a validation of the current study against previously published research. Table 4 represents the influence of the magnetic parameter (M), stretching ratio parameter (γ_1), and Casson fluid parameter (β) on the skin friction at the lower and upper disk. The skin friction is found to increase with the M, $\gamma_1$and β at the bottom disk. The higher the magnetic field, the stronger the Lorentz force; thus, its effect is maximal at the lower disk, whereas at the top disk it decreases. As a result, the surface drag increases at the lower disk. The γ_1 increase the skin friction at both disks. This effect is due to the enhancement of stretching velocity, which results in the skin friction increase at both disks. Furthermore, the variation in β also improve the skin fiction at

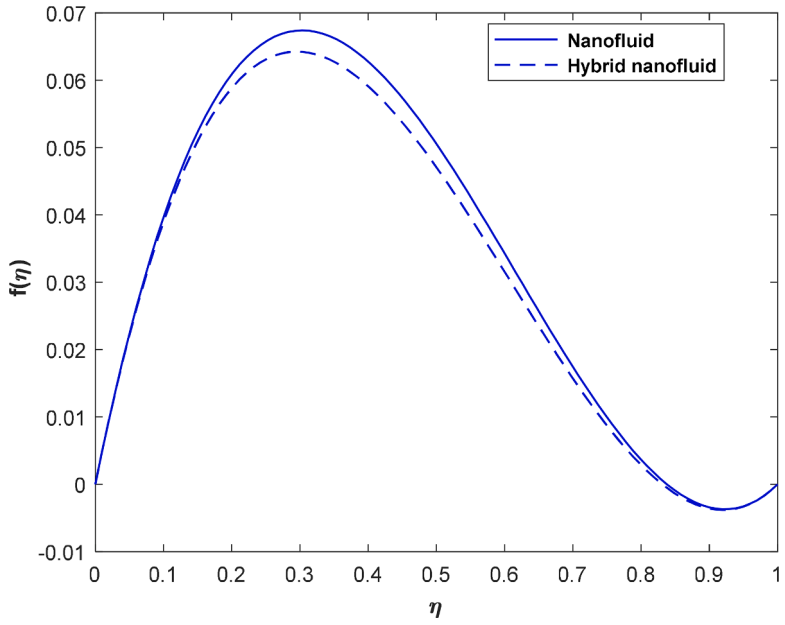

Fig. 22. Effect of nano and hybrid nanoparticles on$f(\eta)$.

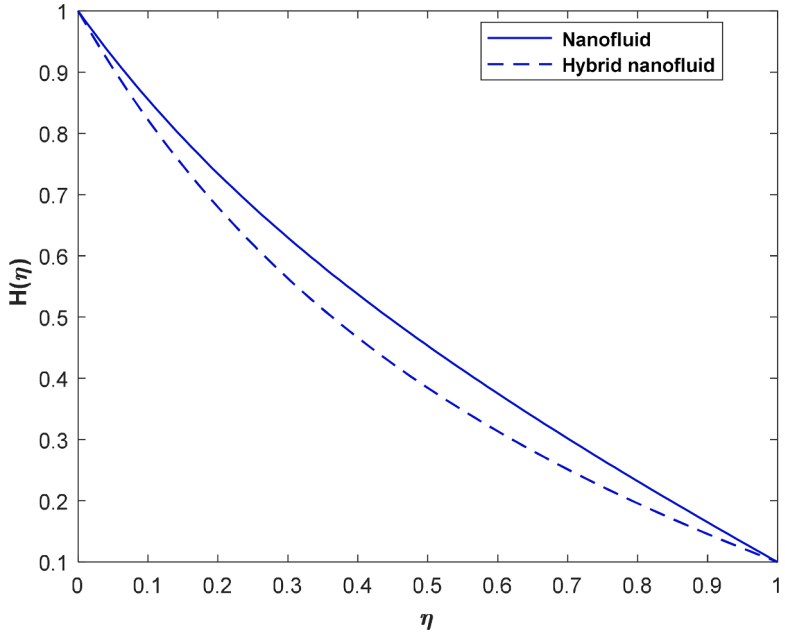

Fig. 23. Effect of nano and hybrid nanoparticles on$H(\eta)$.

lower and top disk. Table 5 presents the influence of thermal radiation parameter (Rd), Biot number (B_1), and Reynolds number (Re) on the Nusselt number at both disks. An increase in thermal radiation enhances internal thermal energy within the fluid, which thickens the thermal boundary layer and hence increase the Nusselt number at the upper disk. A reverse trend is observed at the lower disk. In contrast, increasing the Biot number B_1 intensifies convective heat exchange at the wall. A larger B_1 represents stronger surface convection relative to internal conduction, which steepens the temperature gradient and therefore raises the Nusselt number of both upper and lower disk. Similarly, higher Reynolds number Re strengthens fluid motion and convective transport. Enhanced circulation improves heat extraction from the surface, leading to a consistent rise in the Nusselt number of lower and upper disk. The impact of hybrid nanoparticles on the rate of heat transfer at the lower and upper disks is presented in Table 6. The results demonstrate that the hybrid nanofluid exhibits a significantly higher heat transfer rate compared to the single nanoparticle nanofluid. Physically, the addition of copper $\nabla_{Cu}$and titanium ∇_{Tio_2}nanoparticles to the base fluid enhances its thermophysical properties. The presence of dual nanoparticles increases intermolecular interactions and collision frequency within the fluid. This intensified collision mechanism raises the temperature energy distribution and kinetic activity of the fluid particles, which consequently boosts the heat transport capability of the hybrid nanofluid. Table 7 demonstrates the impact of Schmidt number (Sc) Reynolds number Reand activation energy (E) on the Sherwood number. Increasing Sc corresponds to lower mass diffusivity relative to momentum diffusivity. This reduces species diffusion thickness and produces a steeper concentration gradient at the wall, thereby increasing the Sherwood number at both disks. Higher activation energy suppresses chemical reaction rates inside the fluid, which maintains a stronger

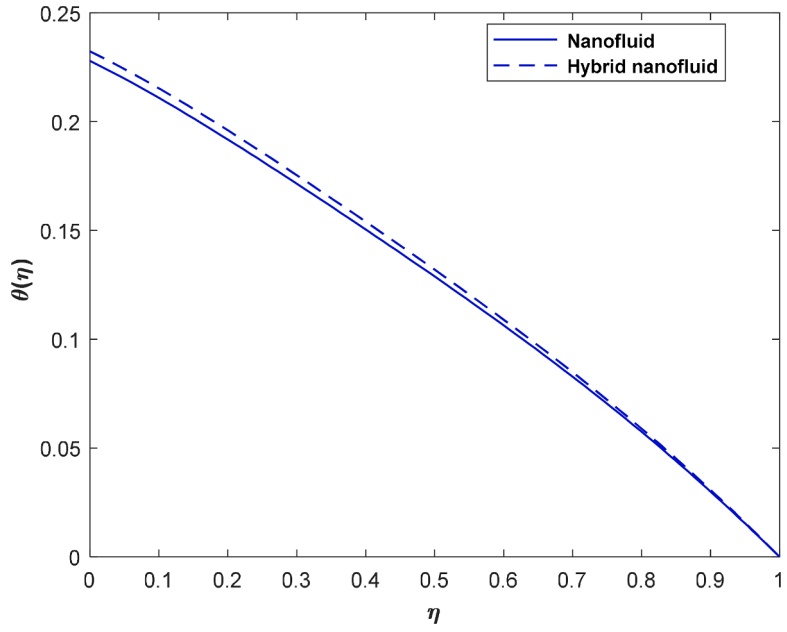

Fig. 24. Effect of nano and hybrid nanoparticles on$\theta(\eta)$.

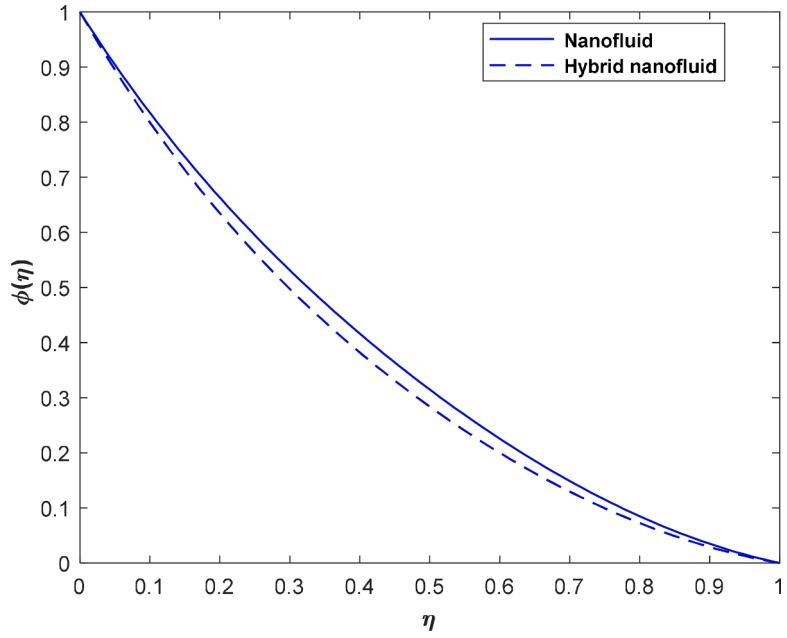

Fig. 25. Effect of nano and hybrid nanoparticles on$\phi(\eta)$.

Table 2
The numerical values of nanoparticles and base fluid [49,50,63].

Physical property	*Cu*	TiO_2	*SA*
$\rho(kg/m^3)$	8933	3.97×10^3	997.1
$C_p(J/kgK)$	385	765	4.179×10^3
$\sigma(\Omega.m^{-1})$	5.96×10^7	1.00×10^{-10}	0.05
$k(W/mK)$	4×10^2	40	0.613
$\beta(1/K)$	1.67×10^{-5}	0.9×10^{-5}	23×10^{-5}
Pr			8.0

concentration difference near the surface and enhances mass transfer. Furthermore, the mass transfer rate also escalates against higher Reynolds number at lower and upper disk.

Table 3
Validation of the present work with the previous result when Re $= 1.0$and$\nabla_{p1} = \nabla_{p2} = M = \gamma_1 = \gamma_2 = 0$, .

	$f''(0)$		$-g'(0)$	
Ω	Hosseinzadeh et al. [52]	Present results	Hosseinzadeh et al. [52]	Present results
−1.0	0.06666265832	0.0666625431	2.000952	2.00094
−0.8	0.08394497836	0.0839449346	1.802594	1.80346
−0.3	0.10394977533	0.10394977521	1.30443	1.30361
−0.0	0.09996773288	0.09996773287	1.004286	1.004162
−0.5	0.06663026596	0.06663026575	0.502619	0.502621

Table 4
Effect of M, and γ_1 on Skin friction.

M	γ_1	Skin friction	
		Lower disk	Upper disk
1.0	0.1	1.2951	0.94616
1.4		1.3599	0.92724
1.9		1.4278	0.90869
	0.2	1.5810	0.96193
	0.3	1.67586	1.00136
	0.4	1.7764	1.04243

Table 5
Effect of Rd,B_1 and Re on Nusselt number.

Rd	B_1	Re	Nusselt number	
			Lower disk	Upper disk
0.4	0.2	1.0	0.84391	0.88319
0.5			0.81859	0.91941
0.6			0.79403	0.95709
	0.3		0.90380	0.92817
	0.4		0.93995	0.97179
	0.5		0.97755	1.01552
		2.0	0.86190	0.88201
		3.0	0.94033	0.94110
		4.0	0.99518	1.00416

Table 6
Effect of nano, and hybrid nanofluids on Nusselt number.

∇_{Cu}	∇_{Tio_2}	Nusselt number	
		Lower	Upper
0.02		0.48910	1.4205
0.03		0.51697	1.4289
0.04		0.54489	1.4372
0.02	0.02	0.54290	1.59096
0.03	0.03	0.57384	1.60037
0.04	0.04	0.60483	1.60966

Table 7
Effect of Sc, E and Reon Sherwood number.

Sc	E	Re	Sherwood number	
			Lower disk	Upper disk
1.0	1.0	2.0	0.55201	1.24915
2.0			0.60002	1.32888
3.0			0.65219	1.41370
	1.2		0.85728	1.20251
	1.3		0.79636	1.25061
	1.4		0.73977	1.30063
		2.5	0.90217	1.25430
		3.5	0.97434	1.32955
		4.5	1.05229	1.40933

7. Conclusion

This study investigates the effects of mixed convection in magnetohydrodynamic (MHD) flow of a non-Newtonian Casson hybrid nanofluid confined between two rotating disks under convective boundary conditions. The analysis incorporates key physical effects such as mixed convection, Joule heating, activation energy, and convective boundary conditions, together with relevant transport parameters, to provide a comprehensive understanding of the systems' coupled thermal and fluid dynamic behavior. To address the complexity of the governing equations, appropriate similarity transformations are employed to reduce the nonlinear partial differential equations (PDEs) to a system of nonlinear ordinary differential equations (ODEs). The resulting system is then solved numerically using MATLAB's bvp4c solver.

The key results are:

1. Increasing Reynolds number strengthens axial and tangential velocities, while a magnetic field suppresses them due to resistive Lorentz forces.
2. Lower-disk stretching enhances axial velocity, whereas upper-disk stretching reduces it; however, upper-disk stretching increases tangential velocity.
3. Rotation boosts transversal velocity, and higher Richardson and Casson parameters increase axial flow.
4. Temperature rises with Reynolds number, magnetic field, Brownian motion, Biot number, Eckert number, and radiation.
5. Concentration increases with activation energy but decreases with Schmidt number, Brownian motion, and chemical reaction.
6. Skin friction grows with lower-disk stretching and the Casson parameter at both disks; magnetic effects increase it at the lower disk but reduce it at the upper disk.
7. Higher nanoparticle volume fraction enhances heat transfer (Nusselt number), especially for hybrid nanofluids.
8. Nusselt number decreases with radiation and Brownian motion but increases with Biot and Eckert numbers.
9. Sherwood number increases with Reynolds and Schmidt numbers at both disks, while activation energy reduces it at the lower disk but raises it at the upper disk.

7.1. Application

The following advanced engineering and biomedical applications can benefit from the study's findings:

- ❖ Biomedical engineering, namely in the modeling of blood-like Casson fluids enhanced with nanoparticles for targeted medication delivery devices, bio-cooling systems, and artificial organs.
- ❖ Thermal management systems include disk-type energy storage devices, revolving heat exchangers, and cooling of rotating machinery.
- ❖ Electromagnetic pumps and metallurgical processes employ magnetohydrodynamic flow control in electrically conducting fluids.
- ❖ SA-based hybrid nanofluids with $(TiO_2 - Cu)$nanoparticles are used in coating and surface engineering for antimicrobial coatings in food packaging and medical implants.
- ❖ Micro-electromechanical systems (MEMS), rotating disk reactors, and renewable energy technologies are examples of energy and power systems where improved heat and mass transfer is essential.

7.2. Future research work

- ❖ Several non-Newtonian fluid models used to expand the current model.
- ❖ In the future, several boundary conditions will be included, including melting heat transfer, slip, zero mass flux and thermal jump.
- ❖ It is possible to apply the Xue and CatteneoChristov thermal conductivity model.
- ❖ Examine the effects of multi-component hybrid nanofluids, nanoparticle size, and shape.
- ❖ Add study of entropy generation, catalytic effects, and several chemical reactions.
- ❖ Verify numerical results using lab-scale or experimental research.

CRediT authorship contribution statement

Sartaj Aziz: Writing – original draft, Conceptualization. **Hakeem Ullah:** Supervision, Methodology. **Mehreen Fiza:** Resources, Project administration. **Ilyas Khan:** Funding acquisition, Formal analysis.

Abdoalrahman S.A. Omer: Software, Funding acquisition, Formal analysis. **Najla A. Mohammed:** Visualization, Resources. **Ibrahim Mahariq:** Validation, Investigation. **Ali Akgül:** Formal analysis, Data curation. **Farkhod Rakhmonov:** Validation, Formal analysis.

Declaration of competing interest

It is to certify that this manuscript contains no material previously published or written by another person, except where due reference has been made to the best of knowledge and belief.

Authors do not have any competing interest regarding the publication of this article.

Data availability

Data will be made available on request.

References

[1] A. Abderrahmane, et al., Second law analysis of a 3D magnetic buoyancy-driven flow of hybrid nanofluid inside a wavy cubical cavity partially filled with porous layer and non-Newtonian layer, Ann. Nucl. Energy 181 (2023) 109511.

[2] S.U.S. Choi, J.A. Eastman, Enhancing thermal conductivity of fluids with nanoparticles, Argonne National Lab.(ANL) (1995).

[3] A.M. Morad, E.S. Selima, A.K. Abu-Nab, Thermophysical bubble dynamics in N-dimensional Al2O3/H2O nanofluid between two-phase turbulent flow, Case Stud. Therm. Eng. 28 (2021) 101527.

[4] A.K. Abu-Nab, A.M. Morad, E.S. Selima, Impact of magnetic-field on the dynamic of gas bubbles in N-dimensions of non-newtonian hybrid nanofluid: analytical study, Phys. Scr. 97 (10) (2022) 105202.

[5] A.K. Abu-Nab, M.H. Omran, A.F. Abu-Bakr, Theoretical analysis of pressure relaxation time in N-dimensional thermally-limited bubble dynamics in Fe3O4/water nanofluids, J. Nanofluids 11 (3) (2022) 410–417.

[6] A.K. Abu-Nab, A.F. Abu-Bakr, Effect of bubble-bubble interaction in Cu− Al2O3/H2O hybrid nanofluids during multibubble growth process, Case Stud. Therm. Eng. 33 (2022) 101973.

[7] S. Jena, S.R. Mishra, P.K. Pattnaik, R.P. Sharma, The nanofluid flow between parallel plates and heat transfer in presence of chemical reaction and porous matrix: nanofluid flow between parallel plates and heat transfer, Lat. Am. Appl. Res.-Int. J. 50 (4) (2020) 283–289.

[8] G.K. Ramesh, S.A. Shehzad, T. Hayat, A. Alsaedi, Activation energy and chemical reaction in Maxwell magneto-nanoliquid with passive control of nanoparticle volume fraction, J. Braz. Soc. Mech. Sci. Eng. 40 (9) (2018) 422.

[9] M. Sheikholeslami, D.D. Ganji, Heat transfer of Cu-water nanofluid flow between parallel plates, Powder. Technol. 235 (2013) 873–879.

[10] G.K. Ramesh, Analysis of active and passive control of nanoparticles in viscoelastic nanomaterial inspired by activation energy and chemical reaction, Phys. A: Stat. Mech. Appl. 550 (2020) 123964.

[11] M.M. Rashidi, S. Abelman, N.F. Mehr, Entropy generation in steady MHD flow due to a rotating porous disk in a nanofluid, Int. J. Heat. Mass Transf. 62 (2013) 515–525.

[12] A. Raptis, C. Perdikis, H.S. Takhar, Effect of thermal radiation on MHD flow, Appl. Math. Comput. 153 (3) (2004) 645–649.

[13] A. Ishak, R. Nazar, I. Pop, Magnetohydrodynamic (MHD) flow and heat transfer due to a stretching cylinder, Energy Convers. Manag. 49 (11) (2008) 3265–3269.

[14] K.U. Rehman, M.Y. Malik, I. Zehra, M.S. Alqarni, Group theoretical analysis for MHD flow fields: a numerical result, J. Braz. Soc. Mech. Sci. Eng. 41 (3) (2019) 156.

[15] G.K. Ramesh, J.K. Madhukesh, Activation energy process in hybrid CNTs and induced magnetic slip flow with heat source/sink, Chin. J. Phys. 73 (2021) 375–390.

[16] A. Arikoglu, I. Ozkol, G. Komurgoz, Effect of slip on entropy generation in a single rotating disk in MHD flow, Appl. Energy 85 (12) (2008) 1225–1236.

[17] J.K. Madhukesh, G.K. Ramesh, S.A. Shehzad, S. Chapi, I.P. Kushalappa, Thermal transport of MHD Casson–Maxwell nanofluid between two porous disks with Cattaneo–Christov theory, Numer. Heat Transf. A: Appl. 85 (12) (2024) 2008–2023.

[18] B. Mohanty, S. Jena, P.K. Pattnaik, MHD nanofluid flow over stretching/shrinking surface in presence of heat radiation using numerical method, Int. J. Emerg. Technol. 10 (2) (2019) 119–125.

[19] B. Mahanthesh, B.J. Gireesha, S.A. Shehzad, A. Rauf, P.B.S. Kumar, Nonlinear radiated MHD flow of nanoliquids due to a rotating disk with irregular heat source and heat flux condition, Phys. B Condens. Matter. 537 (2018) 98–104.

[20] M.D. Shamshuddin, P.S. Rao, S.O. Salawu, A.J. Chamkha, Prevalence of secondary flow due to hall currents on radiative squeezing flow of a CuO-water nanofluid in a rotating channel: numerical prediction, in: Proceedings of the Institution of Mechanical Engineers, Part E: Journal of Process Mechanical Engineering 236, 2022, pp. 1877–1888.

[21] S.O. Salawu, M.D. Shamshuddin, O.A. Bég, Influence of magnetization, variable viscosity and thermal conductivity on Von Karman swirling flow of H2O-FE3O4 and H2O-Mn-ZNFe2O4 ferromagnetic nanofluids from a spinning DISK: smart spin coating simulation, Mater. Sci. Eng. B 279 (2022) 115659.

[22] M.D. Shamshuddin, M.R. Eid, Magnetized nanofluid flow of ferromagnetic nanoparticles from parallel stretchable rotating disk with variable viscosity and thermal conductivity, Chin. J. Phys. 74 (2021) 20–37.

[23] M.G. Reddy, K.V. Reddy, Influence of Joule heating on MHD peristaltic flow of a nanofluid with compliant walls, Procedia Eng. 127 (2015) 1002–1009.

[24] M.M. Maskeen, A. Zeeshan, O.U. Mehmood, M. Hassan, Heat transfer enhancement in hydromagnetic alumina–copper/water hybrid nanofluid flow over a stretching cylinder, J. Therm. Anal. Calorim. 138 (2019) 1127–1136.

[25] N.S. Khashi'ie, N.M. Arifin, I. Pop, N.S. Wahid, Flow and heat transfer of hybrid nanofluid over a permeable shrinking cylinder with joule heating: a comparative analysis, Alex Eng. J. 59 (3) (2020) 1787–1798.

[26] J. Madhu, et al., Influence of quadratic thermal radiation and activation energy impacts over oblique stagnation point hybrid nanofluid flow across a cylinder, Case Stud. Therm. Eng. 60 (2024) 104624.

[27] L. Yan, et al., Dual solutions and stability analysis of magnetized hybrid nanofluid with joule heating and multiple slip conditions, Processes 8 (3) (2020) 332.

[28] T. Ding, W. Ma, Z. Zhao, Review of alumina-based Filler/Epoxy resin composites for thermally conductive materials, Polym. Eng. Sci. (2025).

[29] A.J. Chamkha, A.S. Dogonchi, D.D. Ganji, Magneto-hydrodynamic flow and heat transfer of a hybrid nanofluid in a rotating system among two surfaces in the presence of thermal radiation and joule heating, AIP. Adv. 9 (2) (2019).

[30] S. Li, et al., Aspects of an induced magnetic field utilization for heat and mass transfer ferromagnetic hybrid nanofluid flow driven by pollutant concentration, Case Stud. Therm. Eng. 53 (2024) 103892.

[31] Z. Li, A. Shafee, R. Kandasamy, M. Ramzan, Q.M. Al-Mdallal, Nanoparticle transportation through a permeable duct with Joule heating influence, Microsyst. Technol. 25 (2019) 3571–3580.

[32] I. Ullah, I. Khan, S. Shafie, MHD natural convection flow of casson nanofluid over nonlinearly stretching sheet through porous medium with chemical reaction and thermal radiation, Nanoscale Res. Lett. 11 (2016) 1–15.

[33] S.A. Wajihah, D.S. Sankar, A review on non-Newtonian fluid models for multi-layered blood rheology in constricted arteries, Arch. Appl. Mech. 93 (5) (2023) 1771–1796.

[34] M.D. Shamshuddin, Z. Raizah, N. Akkurt, V.S. Patil, S.M. Eldin, Case study of thermal and solutal aspects on non-Newtonian Prandtl hybrid nanofluid flowing via stretchable sheet: multiple slip solution, Case Stud. Therm. Eng. 49 (2023) 103186.

[35] M.B. Jeelani, A. Abbas, Al2O3-Cu\ethylene glycol-based magnetohydrodynamic non-newtonian Maxwell hybrid nanofluid flow with suction effects in a porous space: energy saving by solar radiation, Symmetry 15 (9) (2023) 1794.

[36] Z. Hussain, F. Aljuaydi, M. Ayaz, S. Islam, Significance of slips and convective conditions towards the non-Newtonian hybrid nanofluid flow over a bi-directional stretching surface, Int. J. Thermofluids 21 (2024) 100537.

[37] M.V. Reddy, R. Meenakumari, G. Sucharitha, F. Ali, S.S. Zafar, P. Lakshminarayana, Heat and mass transfer analysis of conducting non-newtonian nanofluid flows over an elongating sheet with a non-uniform heat source, Mod. Phys. Lett. B (2024) 2450349.

[38] R. Meenakumari, P. Lakshminarayana, K. Vajravelu, G. Sucharitha, Convective heat and mass transfer analysis on Casson nanofluid flow over an inclined permeable expanding surface with modified heat flux and activation energy, Numer. Heat Transf. A: Appl. (2023) 1–20.

[39] M.S. Ilango, P. Lakshminarayana, Effects of double diffusion and induced magnetic field on convective flow of a Casson nanofluid over a stretching surface, Heliyon 10 (10) (2024).

[40] M. Ramzan, T. Mehmood, H. Alotaibi, H.A.S. Ghazwani, T. Muhammad, Comparative study of hybrid and nanofluid flows amidst two rotating disks with thermal stratification: statistical and numerical approaches, Case Stud. Therm. Eng. 28 (2021) 101596.

[41] S.A. Shehzad, F. Mabood, A. Rauf, I. Tlili, Forced convective Maxwell fluid flow through rotating disk under the thermophoretic particles motion, Int. Commun. Heat Mass Transf. 116 (2020) 104693.

[42] S. Noreen, et al., Comparative study of ternary hybrid nanofluids with role of thermal radiation and Cattaneo-Christov heat flux between double rotating disks, Sci. Rep. 13 (1) (2023) 7795.

[43] M. Rahman, M. Turkyilmazoglu, Z. Mushtaq, Effects of multiple shapes for steady flow with transformer oil+ Fe3O4+ TiO2 between two stretchable rotating disks, Appl. Math. Mech. 45 (2) (2024) 373–388.

[44] R. Naveen Kumar, H.B. Mallikarjuna, N. Tigalappa, R.J. Punith Gowda, D. Umrao Sarwe, Carbon nanotubes suspended dusty nanofluid flow over stretching porous rotating disk with non-uniform heat source/sink, Int. J. Comput. Methods Eng. Sci. Mech. 23 (2) (2022) 119–128.

[45] Y. Zhang, J. Jiang, Y. Bai, MHD flow and heat transfer analysis of fractional Oldroyd-B nanofluid between two coaxial cylinders, Comput. Math. Appl. 78 (10) (2019) 3408–3421.

[46] T. Hayat, S. Qayyum, M. Imtiaz, A. Alsaedi, MHD flow and heat transfer between coaxial rotating stretchable disks in a thermally stratified medium, PLoS. One 11 (5) (2016) e0155899.

[47] H. Ullah, et al., Thermal radiation effects of ternary Hybrid nanofluid flow in the activation energy: numerical computational approach, Results. Eng. (2025) 104062.

[48] S.A. Lone, M.A. Alyami, A. Saeed, A. Dawar, P. Kumam, W. Kumam, MHD micropolar hybrid nanofluid flow over a flat surface subject to mixed convection and thermal radiation, Sci. Rep. 12 (1) (2022) 17283.

[49] M. Alghamdi, A. Wakif, T. Thumma, U. Khan, D. Baleanu, G. Rasool, Significance of variability in magnetic field strength and heat source on the radiative-convective motion of sodium alginate-based nanofluid within a Darcy-Brinkman porous structure bounded vertically by an irregular slender surface, Case Stud. Therm. Eng. 28 (Dec. 2021) 101428, https://doi.org/10.1016/J.CSITE.2021.101428.
[50] B. Sharma, S. Kumar, M.K. Paswan, Analytical solution for mixed convection and MHD flow of electrically conducting non-newtonian nanofluid with different nanoparticles: a comparative study, Int. J. Heat Technol. 36 (3) (2018) 987–996.
[51] S.A. Abas, et al., Effects of joule heating on MHD flow of hybrid nanofluid between rotating disks, J. Radiat. Res. Appl. Sci. 18 (2) (2025) 101341.
[52] K. Hosseinzadeh, A.R. Mogharrebi, A. Asadi, M. Sheikhshahrokhdehkordi, S. Mousavisani, D.D. Ganji, Entropy generation analysis of mixture nanofluid (H2O/c2H6O2)–Fe3O4 flow between two stretching rotating disks under the effect of MHD and nonlinear thermal radiation, Int. J. Ambient Energy 43 (1) (2022) 1045–1057.
[53] K. Sudarmozhi, et al., AI-neural network modelling of Williamson blood flow in porous medium Soret-Dufour effects with tetra hybrid nanoparticles, Int. Commun. Heat Mass Transf. 171 (2026) 110107.
[54] H. Ahmad, H.A. Ghazwani, H.I. Elsaeedy, M.M. Mosallem, A.U. Hayat, Numerical algorithm of fourth-grade nanofluid flow with heat transfer consists of aluminum alloys over a riga plate, J. Therm. Anal. Calorim. 150 (19) (2025) 15723–15736.
[55] P.O. Kapustenko, O.P. Arsenyeva, P.S. Varbanov, L.L. Tovazhnyanskyy, Heat transfer intensification in compact heat exchangers with channels of various geometries and size, Int. Commun. Heat Mass Transf. 167 (2025) 109273.
[56] H. Szűcs, Numerical study to investigate the thermal characteristic length with coupled CFD-FEM simulations, Int. J. Heat. Fluid. Flow. 106 (2024) 109312.
[57] Á. Orosz, et al., Exhaustive enumeration of heat exchanger networks with minimum utility consumption using graph-theoretic approach, Energy (2025) 137898.
[58] G. Kovács, S.K. Szürke, S. Fischer, Investigation of convective and radiative heat transfer of 21700 lithium-ion battery cells, Batteries 11 (7) (2025) 246.
[59] T. Morauszki, P. Mandli, Z. Horváth, M.R. Dreyer, Simulation of fluid flow, combustion and heat transfer processes in internal combustion engines, Hung. J. Ind. Chem. (2011) 27–30.
[60] H. Szűcs, Exploring the impact of compressibility on reconstructed porous materials: a numerical study, J. Eng. Res. (2024).
[61] Á. Orosz, F. Friedler, Multiple-solution heat exchanger network synthesis for enabling the best industrial implementation, Energy 208 (2020) 118330.
[62] A. Rashid, M. Ayaz, S. Islam, Mixed convection MHD hybrid nanofluid flow between two parallel rotating discs with joule heating and chemical reactions using bvp4c, Adv. Mech. Eng. 15 (6) (2023) 16878132231179612.
[63] L.A. Lund, A. Asghar, G. Rasool, U. Yashkun, Magnetized casson SA-hybrid nanofluid flow over a permeable moving surface with thermal radiation and joule heating effect, Case Stud. Therm. Eng. 50 (2023) 103510.